THE ASTROPHYSICAL JOURNAL, 536:79–100, 2000 June 10

WEAK LENSING MEASUREMENTS: A REVISITED METHOD AND APPLICATION TO *HUBBLE SPACE TELESCOPE* IMAGES

JASON RHODES
Department of Physics, Princeton University, Jadwin Hall, P.O. Box 708, Princeton, NJ 08544; jrhodes@pupgg.princeton.edu
ALEXANDRE REFREGIER[1]
Department of Astrophysical Sciences, Princeton University, Princeton, NJ 08544; refreg@astro.princeton.edu
AND
EDWARD J. GROTH
Department of Physics, Princeton University, Jadwin Hall, P.O. Box 708, Princeton, NJ 08544; groth@pupgg.princeton.edu
Received 1999 May 7; accepted 2000 January 8

ABSTRACT

The weak distortions produced by gravitational lensing in the images of background galaxies provide a unique method to measure directly the distribution of mass in the universe. However, because the induced distortions are only of a few percent, this technique requires high-precision measurements of the lensing shear and cautious corrections for systematic effects. Kaiser, Squires, & Broadhurst proposed a method to calibrate the ellipticity-shear relation in the presence of point-spread function (PSF) anisotropies and camera distortions. Here, we revisit the Kaiser, Squires, & Broadhurst method in the context of the demanding search for weak lensing by large-scale structure. We show that both the PSF and the camera distortions can be corrected for using source moments, as opposed to ellipticities. We clarify the applicability of some of the approximations made in this method. We derive expressions for the corrections that involve only the galaxy moments. By decomposing the moments into spinors, we derive an explicit relation between the shear and the average ellipticity. We discuss the shortcomings of the method and test its validity using numerical simulations. As an application of the method, we repeat the analysis of the *Hubble Space Telescope* (*HST*) WFPC2 camera performed by Hoekstra et al. We confirm the presence of sizable ($\sim$10%) PSF ellipticities at the edge of the WFPC2 chips. However, we find that the camera distortion is radial, rather than tangential. We also show that the PSF ellipticity varies by as much as 2% over time. We use these measurements to correct the shape of galaxies in the *HST* Survey Strip (the "Groth" Strip). By considering the dependence of the ellipticities on object size, we show that, after corrections, the residual systematic uncertainty for galaxies with radii greater than 0.″15 is about 0.4% when averaged over each chip. We discuss how these results provide good prospects for measuring weak lensing by large-scale structure with deep *HST* surveys.

Subject headings: cosmology: observations — gravitational lensing — techniques: image processing

1. INTRODUCTION

Weak gravitational lensing produces coherent distortions in the images of background galaxies. This effect provides a unique method to measure directly the distribution of mass in the universe (for reviews, see Schneider, Ehlers, & Falco 1992; Narayan & Bartelmann 1996; Mellier 1999). This technique is now routinely used to map the mass of clusters of galaxies (for a review, see Fort & Mellier 1994). A search for weak lensing by large-scale structure is the subject of much recent and on-going theoretical and observational effort (e.g., Villumsen 1995; Stebbins, McKay, & Frieman 1996; Kaiser 1996; Schneider et al. 1997; Van Waerbeke, Bernardeau, & Mellier 1999; Refregier et al. 1998; see Refregier 1999 for a bibliography). The main difficulty lies in the fact that the lensing distortions are small ($\sim$10% for clusters and $\sim$1% for large-scale structure), thus requiring high-precision measurements and tight control of systematic effects.

Kaiser, Squires, & Broadhurst (1995, hereafter KSB) have developed a method to correct for the major systematic effects, namely, the anisotropy of the point-spread function (PSF) and camera distortions, and to calibrate the relation between galaxy ellipticities and lensing shear (for other methods, see also Bonnet & Mellier 1995; Schneider & Seitz 1995). Further elements of their method were presented in Luppino & Kaiser (1997, hereafter LK) and in Hoekstra et al. (1998, hereafter HFKS).

Recently, Kaiser (1999) pointed out that the KSB method had several shortcomings, all stemming from the fact that most PSFs encountered in practice are not sufficiently compact. Kaiser then proposed another method based on the explicit construction of the postconvolution shear operator. Another alternative method was recently proposed by Kuijken (1999). In this different approach, a sheared and convolved isotropic model is fitted to the galaxy image, so as to derive an estimator for the shear. These two methods are promising, but both require complete knowledge of the two-dimensional PSF function, while PSF measurements are sparse because of the finite number of stellar images.

Here, we revisit the KSB method, which has the advantage both of being linear and of relying only on the first multipole moments of the PSF and galaxy images. We focus on the demanding search for weak lensing by large-scale structure. We show that both the PSF and the camera distortions can be corrected for using source moments, as opposed to ellipticities. We

[1] Present address: Institute of Astronomy, Madingley Road, Cambridge, CB3 OHA, UK; ar@ast.cam.ac.uk.

clarify the applicability of some of the approximations made in this method and show how the weight function for stars can be chosen to be different from that for galaxies. We derive expressions for the corrections in term of the moments only. By decomposing the moments into spinors, we derive an explicit relation between the shear and the average ellipticity. We discuss the shortcomings of the method discussed in Kaiser (1999) and Kuijken (1999) and test its validity using numerical simulations.

As an application, we consider weak lensing measurements with the *Hubble Space Telescope* (*HST*). The small PSF and absence of atmospheric seeing makes *HST* an ideal instrument for weak lensing measurements (e.g., Kneib et al. 1996; HFKS). We reproduce the analysis of HFKS, who studied, in detail, the PSF and camera distortion of the WFPC2 camera on board *HST*. We apply these calibrations to the galaxies in the *HST* Survey Strip known as the "Groth Strip" (Groth et al. 1994; Rhodes 1999). In particular, we show how the PSF anisotropy and camera distortions depend on the size of the galaxies. We also discuss the prospects of weak lensing measurements with *HST*. A description of our search for weak lensing by large-scale structure with the Survey Strip will be presented in Rhodes, Refregier, & Groth (2000, in preparation; see also Rhodes 1999).

Because the method is somewhat complex, we provide a practical summary in § 2, in which we point to the results and equations that are of direct practical interest. In § 3, we describe measures of object shapes. Next, in §§ 4 and 5, we show how these measures are affected by the two main classes of deformations, namely, convolutions and distortions, and derive explicit expressions to correct for them. In § 6, we study the effect of shear combined with a convolution on the observed ellipticity. In § 7, we discuss the shortcomings of the method and test its validity using numerical simulations. In § 8, we apply our method to *HST* observations. In particular, we consider measurements of the camera distortion and globular cluster observations and finally apply our results to the Survey Strip. Our conclusions are summarized in § 9.

2. OVERVIEW OF THE METHOD

The purpose of this method is to provide a measure of the shapes of galaxies, to correct for instrumental effects, and to derive an estimate for the weak lensing shear. The images of galaxies are assumed to be altered by two kinds of operations: distortions (sometimes simply called shear), which are intensity-conserving mappings between the source plane and the image plane (see eq. [19]), and convolutions (or smear; see eq. [36]). Specifically, we follow KSB and HFKS and assume that a galaxy image is altered by a distortion due to gravitational lensing, followed by a convolution by a generally anisotropic PSF, and then by a distortion due to the camera optics. Schematically, we can write

$$\text{intrinsic image} \rightarrow \text{lensing}(\partial) \rightarrow \text{PSF}(*) \rightarrow \text{camera}(\partial) \rightarrow \text{observed image}\ , \tag{1}$$

where ∂ and the asterisk symbolize distortions and convolutions, respectively. Here, we revisit the KSB method. We show how to correct for the two latter effects and how to calibrate the sought-after effect of lensing.

The synopsis of our method is shown on Figure 1. Since the method is somewhat complex, we provide here a summary of the method and point to the equations that are of direct practical interest. References to these equations can also be found in this figure.

The basis of the method is to characterize the shapes of galaxies and stars by measuring their multipole moments $\boldsymbol{J}_{ij}$, $\boldsymbol{J}_{ijkl}$, etc. (eq. [5]). To enforce convergence in the presence of image noise, these moments are measured with a weight function $w(\boldsymbol{\theta})$, which we choose to be a Gaussian of width ω (eq. [3]). This choice allows us to write all the expressions for the corrections in terms of the moments. Unlike KSB, we perform all the corrections using moments and postpone the use of ellipticities (eq. [12]) until the last step. This has the advantage of keeping track of the size of the PSF and of the galaxies, and thus of reducing the noise resulting from the corrections, if the PSF size varies across the field.

The first step consists of deriving the distortion matrix $\boldsymbol{\phi}_{ij}^{\text{camera}}$ (eq. [18]) for the camera distortion. HFKS showed that this could be achieved by considering astrometric shift solutions, such as that of Holtzmann et al. (1995) for the WFPC2 camera on *HST*. The resulting shear pattern for WFPC2 is shown on Figure 3. (See discussion in § 8.1 about the difference between this figure and the results of HFKS).

In the second step, we derive the PSF moments from stellar images. For this purpose, the stellar multipole moments $\boldsymbol{J}_{ij}^{*}$ and $\boldsymbol{J}_{ijkl}^{*}$ are measured using an optimally chosen weight-function width ω_{*}. These moments are then corrected for the weight function to provide (an approximation to) the unweighted moments of the PSF (eqs. [54] and [55]). This allows us to use a different weight-function width ω for the galaxies, and thus to improve the sensitivity. The PSF moments are then corrected for the camera distortion (eqs. [24] and [25] with $\omega \rightarrow \infty$). This provides the corrected unweighted PSF moments $\boldsymbol{P}_{ij}$ and $\boldsymbol{P}_{ijkl}$ (eqs. [38] and [51]), that can be then be interpolated across the field using low-order polynomial fits for each component. Figures 8 and 9 show the resulting ellipticities of the WFPC2 PSF derived from two globular clusters, while Figure 10 shows the interpolated PSF ellipticities derived from a combination of the two after the moments have been corrected for weighting and camera distortion.

In the third step, we measure the galaxy moments and correct them for instrumental effects. The galaxy moments $\boldsymbol{J}_{ij}$ and $\boldsymbol{J}_{ijkl}$ are measured using an optimal weight-function width ω. They are then corrected for the camera distortion using $\boldsymbol{\phi}_{ij}^{\text{camera}}$ (eqs. [24] and [25]). The PSF can be decomposed into an anisotropic and an isotropic part (eq. [43]). We correct the galaxy moments $\boldsymbol{J}_{ij}$ for the PSF anisotropy, by expanding in powers of the PSF ellipticity (eq. [46]). Since, by construction, the isotropic part of the PSF is a Gaussian (eq. [44]), we can perform the isotropic correction exactly for $\boldsymbol{J}_{ij}$ (eq. [49]). The fourth order moments $\boldsymbol{J}_{ijkl}$ are then approximately corrected for the PSF (eq. [50]). This provides us with the corrected galaxy moments $\boldsymbol{J}_{ij}^{\omega_g}$ and $\boldsymbol{J}_{ijkl}^{\omega_g}$, which are now effectively weighted by the new weight-function width ω_g (eq. [47]).

The final step consists of measuring the weak lensing shear by averaging over an ensemble of galaxies in a region of the sky. For this purpose, we compute the ellipticity $\boldsymbol{\epsilon}_i$ of each galaxy from its corrected moments $\boldsymbol{J}_{ij}^{\omega_g}$ (eq. [12]). The weak lensing shear $\boldsymbol{\gamma}_i$ is then computed from the average ellipticity $\langle \boldsymbol{\epsilon}_i \rangle$ (eq. [30]). In this last step, one should remember to use ω_g rather than ω as the weight-function width. The relationship between $\boldsymbol{\gamma}_i$ and $\langle \boldsymbol{\epsilon}_i \rangle$ is greatly simplified by considering the rotation

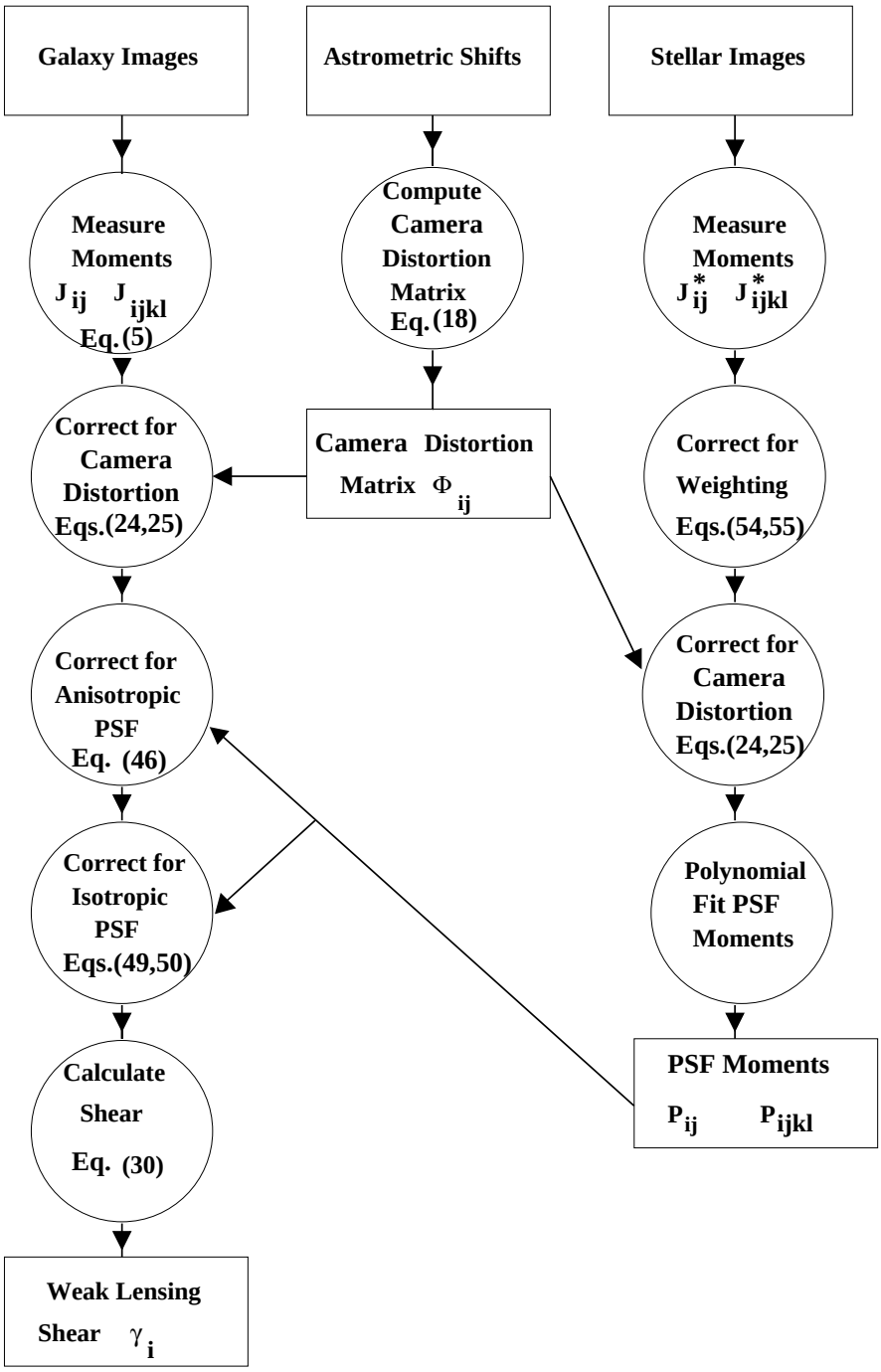

FIG. 1.—Synopsis of the weak lensing measurement method

properties of the multipole moments (see § 3.2). Note that our method avoids the complications of the presmear and postsmear shear susceptibilities discussed in LK and HFKS. In § 8, we discuss the application of our method to the *HST* Survey Strip.

3. SOURCE SHAPE CHARACTERIZATION

In this section, we show how object shapes can be characterized using multipole moments and related quantities. We also study the rotational properties of the moments and decompose them into spinor representations.

3.1. *Moments*

Let us consider a source with intensity $i(\boldsymbol{\theta})$. As a first step, we find the centroid $\boldsymbol{\theta}^0$ of the source by solving

$$\int d^2\boldsymbol{\theta}\,(\theta_i - \theta_i^0) w(\boldsymbol{\theta} - \boldsymbol{\theta}^0) i(\boldsymbol{\theta}) = 0\ , \tag{2}$$

where $w(\boldsymbol{\theta})$ is a weight function introduced to ensure convergence in the presence of noise. In this paper, we will consider a normalized Gaussian weight function,

$$w(\boldsymbol{\theta}) \equiv \frac{1}{2\pi\omega^2}\, e^{-\theta^2/2\omega^2}\,, \tag{3}$$

which has convenient analytical properties. In practice, equation (2) can be solved iteratively, by fixing the weight-function width ω to an initial estimate of the source size (see § 8.3 for a description of our choice of ω for the *HST* Survey Strip).

To characterize the source shape, we consider the weighted multipole moments of the source intensity,

$$I \equiv \int d^2\boldsymbol{\theta}\, w(\boldsymbol{\theta}) i(\boldsymbol{\theta}), \qquad \boldsymbol{I}_{ij} \equiv \int d^2\boldsymbol{\theta}\, \boldsymbol{\theta}_i \boldsymbol{\theta}_j\, w(\boldsymbol{\theta}) i(\boldsymbol{\theta}), \qquad \boldsymbol{I}_{ijk} \equiv \int d^2\boldsymbol{\theta}\, \boldsymbol{\theta}_i \boldsymbol{\theta}_j \boldsymbol{\theta}_k\, w(\boldsymbol{\theta}) i(\boldsymbol{\theta}), \qquad \text{etc}\,. \tag{4}$$

where the origin of the coordinate system was chosen to coincide with $\boldsymbol{\theta}^0$. (By definition, the dipole moment $\boldsymbol{I}_i$ vanishes in this coordinate system). It is usually more convenient to consider the normalized moments

$$\boldsymbol{J}_{ij} \equiv \boldsymbol{I}_{ij}/I, \qquad \boldsymbol{J}_{ijk} \equiv \boldsymbol{I}_{ijk}/I, \qquad \text{etc}\,. \tag{5}$$

The normalized quadrupole moments $\boldsymbol{J}_{ij}$ can be diagonalized as

$$\boldsymbol{J} = \boldsymbol{R}^T(-\alpha)\begin{pmatrix} a^2 & 0 \\ 0 & b^2 \end{pmatrix}\boldsymbol{R}(-\alpha)\,, \tag{6}$$

where a and b are the (weighted) major and minor radii, α is the position angle measured counterclockwise from the positive x-axis, and ^{T} stands for the transpose operation. The rotation matrix $\boldsymbol{R}$ is defined as

$$\boldsymbol{R}(\varphi) \equiv \begin{pmatrix} \cos(\varphi) & -\sin(\varphi) \\ \sin(\varphi) & \cos(\varphi) \end{pmatrix}. \tag{7}$$

Inverting this relation yields

$$(a^2, b^2) = \tfrac{1}{2}\left[J_{11} + J_{22} \pm \sqrt{(J_{11} - J_{22})^2 + 4J_{12}^2}\right], \tag{8}$$

$$\tan 2\alpha = \frac{2J_{12}}{J_{11} - J_{22}}\,. \tag{9}$$

3.2. *Rotational Properties*

To study the rotational properties of the tensors defined above, let us consider a new coordinate system that is rotated counterclockwise by an angle φ from the original positive x-axis. In this new coordinate system, the components $\boldsymbol{J}'_{ij}$ of the normalized quadrupole moments are related to the unrotated components $\boldsymbol{J}_{ij}$ by $\boldsymbol{J}'_{ij} = \boldsymbol{R}_{ik}(-\varphi)\boldsymbol{R}_{jl}(-\varphi)\boldsymbol{J}_{kl}$, and similarly for tensors of higher order, where $\boldsymbol{R}$ is the rotation matrix defined in equation (7). In general, any tensor in 2 dimensions can be decomposed into 2-component (or 1-component for scalars) ℓ-spinors $\boldsymbol{v}_i$, which rotate as

$$\boldsymbol{v}'_i = \boldsymbol{R}_{ij}(-\ell\varphi)\boldsymbol{v}_j, \qquad \ell = 0, \pm 1, \pm, 2, \ldots\,, \tag{10}$$

under this change of coordinates. [These spinors form irreducible representations of $SO(2)$, the rotation group in two dimensions].

For instance, the quadrupole moment $\boldsymbol{J}_{ij}$, which, being symmetric, consists of three independent components, can be decomposed into a scalar

$$d^2 \equiv \tfrac{1}{2}(J_{11} + J_{22}) = \tfrac{1}{2}(a^2 + b^2)\,, \tag{11}$$

which is the mean square radius of the source, and a spin-2 tensor

$$\boldsymbol{\epsilon}_i \equiv \frac{\{J_{11} - J_{22}, 2J_{12}\}}{J_{11} + J_{22}} = \frac{a^2 - b^2}{a^2 + b^2}\{\cos(2\alpha), \sin(2\alpha)\}\,, \tag{12}$$

which is the ellipticity and has been normalized to follow the weak-lensing nomenclature. The component ϵ_1 (ϵ_2) corresponds to stretches and compressions parallel to (at 45° from) the coordinate axes.

By considering infinitesimal rotations, we can also decompose the fourth-order moment $\boldsymbol{J}_{ijkl}$, which has five independent components. We find that it can be decomposed into a scalar,

$$\lambda \equiv (J_{1111} + 2J_{1122} + J_{2222})/(2\,d^2\omega^2)\,, \tag{13}$$

a spin-2 tensor,

$$\mu_1 \equiv (-J_{1111} + J_{2222})/(2\,d^2\omega^2)\,,$$
$$\mu_2 \equiv -2(J_{1112} + J_{1222})/(2\,d^2\omega^2)\,, \tag{14}$$

and a spin-4 tensor,

$$v_1 \equiv (J_{1111} - 6J_{1122} + J_{2222})/(2\,d^2\omega^2)\,,$$
$$v_2 \equiv 4(J_{1112} - J_{1222})/(2\,d^2\omega^2)\,. \tag{15}$$

For future convenience, these spinors have been normalized with the weight-function width ω (eq. [3]) and the scalar d. These decompositions are useful for simplifying tensors that are averaged over an ensemble of randomly oriented galaxies (see § 4.4).

4. DISTORTION

In this section, we study the effect of distortions on the source moments. In practice, distortions arise from the instrument optics and from weak lensing. We show how the former can be corrected and how the latter can be measured by averaging the ellipticities of an ensemble of galaxies.

4.1. *Distortion Matrix*

A distortion is an intensity-conserving mapping between the true position $\boldsymbol{x}$ and the observed position $\boldsymbol{x}'$ of the form

$$\boldsymbol{x}' = \boldsymbol{x}'(\boldsymbol{x}) = \boldsymbol{x} + \delta\boldsymbol{x}(\boldsymbol{x})\,. \tag{16}$$

The observed intensity $i'(\boldsymbol{x})$ is thus related to the true intensity $i(\boldsymbol{x})$ by

$$i'(\boldsymbol{x}') = i(\boldsymbol{x}(\boldsymbol{x}'))\,. \tag{17}$$

The local properties of the distortion are quantified by the distortion matrix $\boldsymbol{\phi}$, which is defined as

$$\boldsymbol{\phi}_{ij} \equiv \begin{pmatrix} \kappa + \gamma_1 & \gamma_2 + \rho \\ \gamma_2 - \rho & \kappa - \gamma_1 \end{pmatrix} \equiv \left| \frac{\partial(\delta\boldsymbol{x}_i)}{\partial\boldsymbol{x}_j} \right|_{\boldsymbol{x}^0}\,, \tag{18}$$

where κ is the convergence, γ_i the shear, and ρ the rotation parameter. The convergence κ describes overall rescalings, and the shear components γ_1 and γ_2 describe contractions and dilations parallel to, and at 45° from, the coordinate axes. In the case of weak lensing, $\boldsymbol{\phi}$ is directly related to the second-order derivative of the gravitational potential projected along the line of sight. While the rotation parameter ρ is expected to be negligible for weak lensing, it is generally not so for instrumental distortions.

Let us consider a true position $\boldsymbol{x} = \boldsymbol{x}^0 + \Delta\boldsymbol{x}$, which is close to a reference position $\boldsymbol{x}^0$ (e.g., the centroid of a source). For small distortions (i.e., if the offset Δx is small compared to the scale on which the distortion mapping varies), the corresponding distorted position is given by $\boldsymbol{x}'_i = \boldsymbol{x}_i^{0\prime} + (\boldsymbol{\delta}_{ij} + \boldsymbol{\phi}_{ij})\Delta\boldsymbol{x}_j + O(\boldsymbol{\phi}^2)$, where $\boldsymbol{x}_i^{0\prime} \equiv \boldsymbol{x}'_i(\boldsymbol{x}^0)$ and $O(\boldsymbol{\phi}^2)$ denotes higher order derivatives of the distortion mapping. Similarly, the true position corresponding to a distorted position $\boldsymbol{x}' = \boldsymbol{x}^{0\prime} + \Delta\boldsymbol{x}'$, is given by $\boldsymbol{x}_i = \boldsymbol{x}_i^0 + (\boldsymbol{\delta}_{ij} - \boldsymbol{\phi}_{ij})\Delta\boldsymbol{x}'_j + O(\boldsymbol{\phi}^2)$. By inserting this expression in equation (17) and by letting $\boldsymbol{x}_i^{0\prime} = \boldsymbol{x}_i^0 \equiv 0$ and $\boldsymbol{\theta}_i \equiv \Delta\boldsymbol{x}'_i$, we obtain

$$i'(\boldsymbol{\theta}_i) = i(\boldsymbol{\theta}_i - \boldsymbol{\phi}_{ij}\,\boldsymbol{\theta}_j) + O(\boldsymbol{\phi}^2)\,. \tag{19}$$

4.2. *Effect of Distortion on the Source Moments*

The quadrupole moment $\boldsymbol{I}'_{ij}$ (eq. [4]) for the distorted image $i'(\boldsymbol{\theta})$ (eq. [19]) is given by

$$\boldsymbol{I}'_{ij} = \int d^2\boldsymbol{\theta}\,\boldsymbol{\theta}_i\,\boldsymbol{\theta}_j\,w(\boldsymbol{\theta})i(\boldsymbol{\theta}_k - \boldsymbol{\phi}_{kl}\,\boldsymbol{\theta}_l) + O(\boldsymbol{\phi}^2)\,. \tag{20}$$

After Taylor expanding and integrating by parts we get, for a Gaussian weight function (eq. [3]), $\boldsymbol{I}'_{ij} = \boldsymbol{I}_{ij} + 2\boldsymbol{I}_{k[i}\,\boldsymbol{\phi}_{j]k} + \boldsymbol{I}_{ij}\,\boldsymbol{\phi}_{kk} - \omega^{-2}\boldsymbol{I}_{ijkl}\,\boldsymbol{\phi}_{kl} + O(\boldsymbol{\phi}^2)$, where the unprimed moments correspond to the undistorted moments. Similarly, the distorted monopole moment is related to the undistorted moments by $I' = I + I\boldsymbol{\phi}_{kk} - \omega^{-2}I_{kl}\,\boldsymbol{\phi}_{kl} + O(\boldsymbol{\phi}^2)$. As a result, the distorted normalized moments (eq. [5]) are given by

$$\boldsymbol{J}'_{ij} = \boldsymbol{J}_{ij} + \boldsymbol{D}_{ijkl}\,\boldsymbol{\phi}_{kl} + O(\boldsymbol{\phi}^2)\,, \tag{21}$$

where the distortion susceptibility tensor $\boldsymbol{D}_{ijkl}$ is given by

$$\boldsymbol{D}_{ijkl} = \boldsymbol{D}_{ijkl}(\boldsymbol{J}) = 2\delta_{k[i}\,\boldsymbol{J}_{j]l} + \omega^{-2}(\boldsymbol{J}_{ij}\,\boldsymbol{J}_{kl} - \boldsymbol{J}_{ijkl})\,. \tag{22}$$

The brackets denote the symmetrizer, which, for an arbitrary tensor $A_{i_1\,i_2\,\ldots\,i_n}$ of rank n, is defined by

$$A_{[i_1\,i_2\,\ldots\,i_n]} \equiv \frac{1}{n!}\,(A_{i_1\,i_2\,\ldots\,i_n} + \text{all } n!\text{ permutations of } \{i_1, i_2, \ldots, i_n\})\,. \tag{23}$$

Inverting equation (21) yields

$$\boldsymbol{J}_{ij} = \boldsymbol{J}'_{ij} - \boldsymbol{D}'_{ijkl}\,\boldsymbol{\phi}_{kl} + O(\boldsymbol{\phi}^2)\,, \tag{24}$$

where $\boldsymbol{D}'_{ijkl} = \boldsymbol{D}_{ijkl}(\boldsymbol{J}')$. This expression can be used to correct the normalized moments for a known distortion.

4.3. *Correction for the Fourth-Order Moments*

In principle, the correction for the fourth-order moments $\boldsymbol{J}_{ijkl}$ can be derived in a similar way. However, when the weight function $w(\boldsymbol{\theta})$ is taken into account, the resulting expressions contain sixth-order moments and are very cumbersome. As we

will see in § 8, it is sufficient, in practice, to consider the unweighted ($\omega \to \infty$) corrections to $\boldsymbol{J}_{ijkl}$. In this approximation, the corrected fourth-order moments $\boldsymbol{J}_{ijkl}$ are related to the distorted moments $\boldsymbol{J}'_{ijkl}$ by

$$\boldsymbol{J}_{ijkl} \simeq \boldsymbol{J}'_{ijkl} - 4J'_{m[ijk}\,\boldsymbol{\phi}_{l]m} + O(\boldsymbol{\phi}^2)\,, \tag{25}$$

where, as before, the brackets denote the symmetrizer (eq. [23]). This expression can be used to correct $\boldsymbol{J}'_{ijkl}$ for instrumental distortions.

4.4. *Measurement of the Shear*

We now show how the gravitational shear can be measured by averaging over galaxy ellipticities. For this purpose, we consider galaxy moments that have been corrected for all instrumental effects, i.e., from instrumental distortion and PSF convolution, using the prescriptions presented in the other sections of this paper. The effect of a weak general distortion $\boldsymbol{\phi}_{ij}$ (eq. [18]) on the (corrected) ellipticity of a galaxy can be derived by substituting the distorted moments $\boldsymbol{J}'_{ij}$ (eq. [21]) into the definition of the ellipticity $\boldsymbol{\epsilon}_i$ (eq. [12]). This results in a relation between the distorted ellipticity $\boldsymbol{\epsilon}_i$ and the distortion parameters $\delta_i \equiv \{\kappa, \gamma_1, \gamma_2, \rho\}$ of the form $\boldsymbol{\epsilon}_i = \boldsymbol{A}_{ij}\boldsymbol{\delta}_j + O(\boldsymbol{\phi}^2)$, with

$$\boldsymbol{A}_{ij} \equiv \begin{pmatrix} \mu_1 + \lambda\epsilon_1 & 2 - 2\epsilon_1^2 - \epsilon_1\mu_1 - \frac{1}{2}\lambda - \frac{1}{2}\nu_1 & -2\epsilon_1\epsilon_2 - \epsilon_1\mu_2 - \frac{1}{2}\nu_2 & 2\epsilon_2 \\ \mu_2 + \lambda\epsilon_2 & -2\epsilon_1\epsilon_2 - \epsilon_2\mu_1 - \frac{1}{2}\nu_2 & 2 - 2\epsilon_2^2 - \epsilon_2\mu_2 - \frac{1}{2}\lambda + \frac{1}{2}\nu_1 & -2\epsilon_1 \end{pmatrix}, \tag{26}$$

where γ, $\boldsymbol{\mu}_i$, and ν_i are the spinors defined in § 3.2. Note that ρ is kept here for completeness but is expected to vanish for weak lensing distortions.

To measure the shear γ_i, we then average over an ensemble of galaxies that are assumed to be randomly oriented, intrinsically. Thus, all we need is the rotational average of the above relation, which we write as $\langle\boldsymbol{\epsilon}_i\rangle = \langle\boldsymbol{A}_{ij}\rangle\boldsymbol{\delta}_j + O(\boldsymbol{\phi}^2)$. After discarding all terms that are not rotationally invariant, we obtain

$$\langle\boldsymbol{A}_{ij}\rangle = \begin{pmatrix} 0 & G_1 & -G_2 & 0 \\ 0 & G_2 & G_1 & 0 \end{pmatrix}, \tag{27}$$

where

$$G_1 \equiv 2 - \langle\epsilon^2\rangle - \tfrac{1}{2}\langle\lambda\rangle - \tfrac{1}{2}\langle\boldsymbol{\epsilon}\cdot\boldsymbol{\mu}\rangle, \qquad G_2 \equiv \tfrac{1}{2}\langle\boldsymbol{\epsilon}\times\boldsymbol{\mu}\rangle\,, \tag{28}$$

and $\epsilon^2 \equiv \epsilon_1^2 + \epsilon_2^2$, $\boldsymbol{\epsilon}\cdot\boldsymbol{\mu} \equiv \epsilon_1\mu_1 + \epsilon_2\mu_2$, and $\boldsymbol{\epsilon}\times\boldsymbol{\mu} \equiv \epsilon_1\mu_2 - \epsilon_2\mu_1$. Note that, to this order, the convergence κ and the rotation parameter ρ do not affect the mean ellipticity $\langle\boldsymbol{\epsilon}_i\rangle$.

Since we do not expect the galaxy population to have a preferred handedness, we can also discard terms that are not parity invariant. It is easy to check that $\boldsymbol{\epsilon}\times\boldsymbol{\mu}$ is such a term since it changes sign when it is transformed to a left-handed coordinate system (e.g., $x \to x$, $y \to -y$). We are therefore left with a remarkably simple relation between the mean ellipticity $\langle\boldsymbol{\epsilon}_i\rangle$ and the shear γ_i given by

$$\langle\boldsymbol{\epsilon}_i\rangle = G\gamma_i + O(\boldsymbol{\phi}^2)\,, \tag{29}$$

where $G \equiv G_1$ is the shear susceptibility. This expression agrees with equation (B13) in KSB, as corrected by HFKS. The inverse relation,

$$\gamma_i = E\langle\boldsymbol{\epsilon}_i\rangle + O(\boldsymbol{\phi}^2)\,, \tag{30}$$

where $E \equiv G^{-1}$ can be used to measure the shear from the averaged ellipticity.

4.5. *Special Cases*

Unweighted moments.—In this case, the effect of a general distortion $\boldsymbol{\phi}_{ij}$ (eq. [18]) on the ellipticity is more tractable. We find that the distorted ellipticity $\boldsymbol{\epsilon}'_i$ is given by

$$\boldsymbol{\epsilon}'_i = \boldsymbol{\epsilon}_i + 2(\boldsymbol{\delta}_{ij} - \boldsymbol{\epsilon}_i\boldsymbol{\epsilon}_j)\gamma_j + 2\boldsymbol{e}_{ij}\boldsymbol{\epsilon}_j\rho + O(\boldsymbol{\phi}^2)\,, \tag{31}$$

where $\boldsymbol{\epsilon}_i$ is the undistorted ellipticity and the Levi-Cività symbol $\boldsymbol{e}_{ij}$ is defined by $e_{11} = e_{22} = 0$, $e_{12} = -e_{21} = 1$. When averaged over an ensemble of randomly distributed sources, this reduces to

$$\langle\boldsymbol{\epsilon}'_i\rangle = (2 - \langle\boldsymbol{\epsilon}^2\rangle)\gamma_i + O(\boldsymbol{\phi}^2)\,, \tag{32}$$

in agreement with equation (29) in the $\omega \to \infty$ limit.

Circular source, unweighted moments.—If we make the further simplifying assumption that the undistorted source is circular ($\boldsymbol{\epsilon} = 0$), the distorted ellipticity (eq. [31]) becomes

$$\boldsymbol{\epsilon}'_i \equiv \boldsymbol{\epsilon}_i^{\boldsymbol{\phi}} = 2\gamma_i + O(\boldsymbol{\phi}^2)\,. \tag{33}$$

It is useful to plot the distortion ellipticity $\boldsymbol{\epsilon}$ (rather than γ_i) as a function of position on the chip, as a measure of the effect of the camera distortion (see Fig. 3).

Radial displacement.—Let us consider the case where the displacement field (eq. [16]) is radial, i.e., where $\delta\boldsymbol{x} = f(x)(\boldsymbol{x}/x)$, where $x \equiv |\boldsymbol{x}|$ and $f(x)$ is an arbitrary function. It is easy to show that, in this case, the distortion tensor (eq. [18]) is

$$\phi_{ij} = \left(\frac{df}{dx} - \frac{f}{x}\right)\frac{\boldsymbol{x}_i\boldsymbol{x}_j}{x^2} + \frac{f}{x}\,\boldsymbol{\delta}_{ij}\,. \tag{34}$$

The corresponding distortion ellipticity (eq. [33]) is

$$\epsilon^{\phi} = \left(\frac{df}{dx} - \frac{f}{x}\right)\epsilon^{x} , \tag{35}$$

where $\epsilon^{x} \equiv \{x_1^2 - x_2^2, 2x_1 x_2\}/(x_1^2 + x_2^2)$ is the unit radial ellipticity field. From this expression, it is easy to see that ϵ^{ϕ} will be radial (tangential) if $(df/dx - f/x)$ is positive (negative).

5. CONVOLUTION

In this section, we study the effect of convolution by a weakly anisotropic PSF on the source moments. The PSF can be decomposed into an isotropic and an anisotropic part. We show how each part can be corrected for and how the PSF moments can be derived from stellar images.

5.1. *Effect of Convolution on the Source Moments*

Let us consider the case where the true galaxy image $i(\boldsymbol{\theta})$ is convolved by a kernel $p(\boldsymbol{\theta})$. We take $p(\boldsymbol{\theta})$ to be normalized so that $\int d^2\boldsymbol{\theta}\, p(\boldsymbol{\theta}) \equiv 1$ and centered so that $\int d^2\boldsymbol{\theta}\, \boldsymbol{\theta}_i\, p(\boldsymbol{\theta}) \equiv 0$. The observed image is given by

$$i'(\boldsymbol{\theta}) = \int d^2\boldsymbol{\theta}'\, p(\boldsymbol{\theta} - \boldsymbol{\theta}')i(\boldsymbol{\theta}') , \tag{36}$$

so that the observed moments are

$$\boldsymbol{I}'_{ij} = \int d^2\boldsymbol{\theta} \int d^2\boldsymbol{\theta}'\, \boldsymbol{\theta}_i \boldsymbol{\theta}_j\, w(\boldsymbol{\theta}) p(\boldsymbol{\theta} - \boldsymbol{\theta}')i(\boldsymbol{\theta}') . \tag{37}$$

There are three angular scales in this equation, namely, ω, g, and a, corresponding to the size of the weight function w, the PSF kernel p, and the (unconvolved) source i, respectively. To simplify this expression, we need to make an expansion with respect to the ratio between two of these angular scales. We choose to expand with respect to g/ω, thereby assuming that the window function width is much larger than that of the PSF. In practice, the weight function scale is always chosen to be at least as large as the source size, i.e., $\omega \gtrsim a$. To be conservative, we thus take $a \sim \omega$ to collect the terms in the expansion. KSB instead, effectively expanded in powers of $g/(a^2 + g^2)^{1/2}$. It is interesting to note that the expression we derive below for $\boldsymbol{I}'_{ij}$ is nevertheless identical to theirs, to second order in g/ω.

After a change of variable ($\boldsymbol{\theta}'' \equiv \boldsymbol{\theta} - \boldsymbol{\theta}'$) and a Taylor expansion of $w(\boldsymbol{\theta}' + \boldsymbol{\theta}'')$ about $\boldsymbol{\theta}'$, the previous equation becomes $\boldsymbol{I}'_{ij} = \boldsymbol{I}_{ij} + I\boldsymbol{P}_{ij} - (2/\omega^2)I_{k[i}\boldsymbol{P}_{j]k} - [1/(2\omega^2)]\boldsymbol{I}_{ij}\boldsymbol{P}_{kk} + [1/(2\omega^4)]\boldsymbol{I}_{ijkl}\boldsymbol{P}_{kl} + O(g^4/\omega^2)$, where the brackets stand for the symmetrizer (eq. [23]) and I and $\boldsymbol{I}_{ijkl}$ are the (undistorted) weighted moments (eq. [4]). As before, we take the weight function $w(\boldsymbol{\theta})$ to be a normalized Gaussian (eq. [3]). The moments $\boldsymbol{P}_{ij}$ are the (unweighted) moments of the convolution kernel, i.e.,

$$\boldsymbol{P}_{ij} \equiv \int d^2\boldsymbol{\theta}\, \boldsymbol{\theta}_i \boldsymbol{\theta}_j\, p(\boldsymbol{\theta}) . \tag{38}$$

As stated above, this agrees, to this order, with KSB, as corrected for a factor of $\frac{1}{2}$ by HFKS. In § 5.6, we will show how the unweighted PSF moments $\boldsymbol{P}_{ij}$ can be derived from weighted stellar moments. In a similar fashion, it is easy to show that the convolved monopole moment is $I' = I - [1/(2\omega^2)]I\boldsymbol{P}_{kk} + [1/(2\omega^4)]\boldsymbol{I}_{kl}\boldsymbol{P}_{kl} + O(g^4/\omega^4)$. As a result, the convolved normalized moments (eq. [5]) are given by

$$\boldsymbol{J}'_{ij} = \boldsymbol{J}_{ij} + \boldsymbol{C}_{ijkl}\boldsymbol{P}_{kl} + O\left(\frac{g^4}{\omega^2}\right) , \tag{39}$$

where the convolution susceptibility tensor $\boldsymbol{C}_{ijkl}$ is given by

$$\boldsymbol{C}_{ijkl} = \boldsymbol{C}_{ijkl}(\boldsymbol{J}) = \boldsymbol{\delta}_{ik}\boldsymbol{\delta}_{jl} - \frac{2}{\omega^2}\boldsymbol{J}_{k[i}\boldsymbol{\delta}_{j]l} + \frac{1}{2\omega^4}(\boldsymbol{J}_{ijkl} - \boldsymbol{J}_{ij}\boldsymbol{J}_{kl}) . \tag{40}$$

Inverting these equations yields

$$\boldsymbol{J}_{ij} = \boldsymbol{J}'_{ij} - \boldsymbol{C}'_{ijkl}\boldsymbol{P}_{kl} + O\left(\frac{g^4}{\omega^2}\right) , \tag{41}$$

where $\boldsymbol{C}'_{ijkl} = \boldsymbol{C}_{ijkl}(\boldsymbol{J}')$. The last two equations can be used to correct the observed moments $\boldsymbol{J}'_{ij}$ for the PSF, and require knowledge of only the observed quadrupole and fourth-order moments, $\boldsymbol{J}_{ij}$ and $\boldsymbol{J}_{ijkl}$, of the galaxy, and of the quadrupole moments $\boldsymbol{P}_{ij}$ of the PSF. We now show how this approximation can be used to correct for a weakly anisotropic PSF.

5.2. *Correction for the PSF*

In practice, it is often required to include galaxies with size a (and therefore weight-function width ω) only marginally larger than the PSF size g. The PSF correction given by equation (41) is thus not directly applicable, as the expansion series do not

converge sufficiently fast. We can nevertheless apply the above correction scheme when the PSF is weakly anisotropic and sufficiently compact. In this case, we write the unweighted PSF moments as

$$\boldsymbol{P}_{ij} = g^2 \begin{pmatrix} 1+\epsilon_1^p & \epsilon_2^p \\ \epsilon_2^p & 1-\epsilon_1^p \end{pmatrix}, \tag{42}$$

where g is the PSF radius and ϵ_i^p is the PSF ellipticity, which is assumed to be small. We can then decompose the kernel $p(\boldsymbol{\theta})$ into the convolution of an isotropic part $p^i(\boldsymbol{\theta})$ with an anisotropic part $p^a(\boldsymbol{\theta})$, as

$$p = p^i * p^a . \tag{43}$$

It is easy to show that this implies that $\boldsymbol{P}_{ij} = \boldsymbol{P}^i_{ij} + \boldsymbol{P}^a_{ij}$, where $\boldsymbol{P}^i_{ij}$ and $\boldsymbol{P}^a_{ij}$ are the unweighted moments of p^i and p^a, respectively. Without loss of generality, we further require that

$$p^i(\boldsymbol{\theta}) \equiv \frac{1}{2\pi g^2} e^{-\theta^2/(2g^2)} \tag{44}$$

be a normalized circular Gaussian with standard deviation g. This implies that

$$\boldsymbol{P}^i_{ij} = g^2 \boldsymbol{\delta}_{ij}, \qquad \text{and} \qquad \boldsymbol{P}^a_{ij} = g^2 \begin{pmatrix} \epsilon_1^p & \epsilon_2^p \\ \epsilon_2^p & -\epsilon_1^p \end{pmatrix} . \tag{45}$$

We now show how to correct each of these components in turn.

5.3. *Anisotropic Correction*

If we consider a convolution with the anisotropic kernel $p^a(\boldsymbol{\theta})$ alone, the corrected moments (eq. [41]) become

$$\boldsymbol{J}_{ij} = \boldsymbol{J}'_{ij} - \boldsymbol{C}'_{ijkl} \boldsymbol{P}^a_{kl} + O\left[\frac{(g\epsilon^p)^4}{\omega^2}\right], \tag{46}$$

where, as before, $\boldsymbol{C}'_{ijkl} = \boldsymbol{C}_{ijkl}(\boldsymbol{J}')$ is defined in equation (40). The residual terms are now suppressed by the factor $(\epsilon^p)^4$ and are thus negligible in practice.

5.4. *Isotropic Correction*

As explained earlier, the above approximation cannot be applied to correct for the isotropic part of the PSF. However, since, by construction, the isotropic part p^i of the kernel is a Gaussian, we can perform the isotropic correction exactly. Indeed, by inserting the form of p^i (eq. [44]) into equation (37) and by integrating twice, we find the convolved moments to be $\boldsymbol{I}^{\omega'}_{ij} = g^2_\omega I^{\omega_g} \boldsymbol{\delta}_{ij} + (g_\omega/g)^4 \boldsymbol{I}^{\omega_g}_{ij}$ where

$$\omega_g^2 \equiv \omega^2 + g^2, \qquad g_\omega^{-2} \equiv g^{-2} + \omega^{-2} , \tag{47}$$

and the superscripts $^\omega$ and $^{\omega_g}$ in the moments I, $\boldsymbol{I}_{ij}$, and $\boldsymbol{I}'_{ij}$ indicate the standard deviation of their respective weight functions. The convolved monopole moment is simply $I^{\omega'} = I^{\omega_g}$. Consequently, the convolved normalized moments are

$$\boldsymbol{J}^{\omega'}_{ij} = \left(\frac{g_\omega}{g}\right)^4 \boldsymbol{J}^{\omega_g}_{ij} + g^2_\omega \boldsymbol{\delta}_{ij} . \tag{48}$$

This convenient relation allows us to relate the convolved moments $\boldsymbol{J}^{\omega'}_{ij}$ with the unconvolved moments $\boldsymbol{J}^{\omega_g}_{ij}$, but this time weighted with the wider weight standard deviation ω_g. For later reference, we explicitly write the inverse relation

$$\boldsymbol{J}^{\omega_g}_{ij} = \left(\frac{g}{g_\omega}\right)^4 (\boldsymbol{J}^{\omega'}_{ij} - g^2_\omega \boldsymbol{\delta}_{ij}) , \tag{49}$$

which can be used to correct for the isotropic part of the PSF.

5.5. *Correction for the Fourth-Order Moments*

As in the case of distortions (§ 4.3), the general expression for the correction of the fourth-order moments $\boldsymbol{J}_{ijkl}$ for convolutions contains sixth-order moments and is very cumbersome. Here again, it is usually sufficient to consider the unweighted ($\omega \to \infty$) corrections to $\boldsymbol{J}_{ijkl}$. With this approximation, the corrected moments $\boldsymbol{J}_{ijkl}$ are related to the convolved moments $\boldsymbol{J}'_{ij}$ and $\boldsymbol{J}'_{ijkl}$ by

$$\boldsymbol{J}_{ijkl} \simeq \boldsymbol{J}'_{ijkl} - \boldsymbol{P}_{ijkl} - 6P_{[ij} J'_{kl]} + 6P_{[ij} P_{kl]} , \tag{50}$$

where

$$\boldsymbol{P}_{ijkl} \equiv \int d^2\boldsymbol{\theta}\, \boldsymbol{\theta}_i \boldsymbol{\theta}_j \boldsymbol{\theta}_k \boldsymbol{\theta}_l\, p(\boldsymbol{\theta}) \tag{51}$$

is the (unweighted) fourth-order PSF moment and the brackets denote the symmetrizer (eq. [23]). This expression can be used to correct $\boldsymbol{J}'_{ijkl}$ for convolutions. In the next section, we will show how $\boldsymbol{P}_{ijkl}$ can be estimated from stellar moments.

5.6. *Measurement of the PSF with Stars*

Stars are pointlike and therefore have intensity profiles given by $i^*(\boldsymbol{\theta}) = S\delta^{(2)}(\boldsymbol{\theta})$, where S is the flux. The intrinsic moments (eq. [4]) of a star are thus $I^* = Sw_*(0)$ and $\boldsymbol{I}^*_{ij} = \boldsymbol{J}^*_{ij} = 0$. We allow for the possibility that the weight function, $w_*(\boldsymbol{\theta})$, for the stars is different than that for galaxies, $w(\boldsymbol{\theta})$. After convolution (see eq. [41] and above), the moments become $I^{*\prime} = I^* - 1/(2\omega_*^2)I^*\boldsymbol{P}_{kk} + O(g^4/\omega_*^4)$ and $\boldsymbol{I}^{*\prime}_{ij} = I^*\boldsymbol{P}_{ij} - 1/(2\omega_*^2)I^*\boldsymbol{P}_{ijkk} + O(g^6/\omega_*^4)$, where $\boldsymbol{P}_{ijkl}$ was defined in equation (51). As a result, the normalized moments become

$$\boldsymbol{J}^{*\prime}_{ij} = \boldsymbol{P}_{ij} + \frac{1}{2\omega_*^2}\left(\boldsymbol{P}_{ij}\boldsymbol{P}_{kk} - \boldsymbol{P}_{ijkk}\right) + O\left(\frac{g^6}{\omega_*^4}\right). \tag{52}$$

It is also easy to show that the observed fourth-order moments are given by $\boldsymbol{I}^{*\prime}_{ij\,kl} = I^*\boldsymbol{P}_{ijkl} + O(g^6/\omega_*^2)$, while their normalized version is

$$\boldsymbol{J}^{*\prime}_{ijkl} = \boldsymbol{P}_{ijkl} + O\left(\frac{g^6}{\omega_*^2}\right). \tag{53}$$

We can invert these equations to obtain

$$\boldsymbol{P}_{ij} = \boldsymbol{J}^{*\prime}_{ij} - \frac{1}{2\omega_*^2}\left(\boldsymbol{J}^{*\prime}_{ij}\boldsymbol{J}^{*\prime}_{kk} - \boldsymbol{J}^{*\prime}_{ijkk}\right) + O\left(\frac{g^6}{\omega_*^4}\right) \tag{54}$$

and

$$\boldsymbol{P}_{ijkl} = \boldsymbol{J}^{*}_{ijkl} + O\left(\frac{g^6}{\omega_*^2}\right). \tag{55}$$

With these expressions, the unweighted PSF moments $\boldsymbol{P}_{ij}$ and $\boldsymbol{P}_{ijkl}$ can be derived from the observed stellar moments $\boldsymbol{J}^{*\prime}_{ij}$ and $\boldsymbol{J}^{*\prime}_{ij\,kk}$. These can then be corrected for the camera distortion using equations (24) and (25) with $\omega \to \infty$ and then used in equations (46), (49), and (50) to correct the galaxy moments. For this purpose, $\boldsymbol{P}_{ij}$ and $\boldsymbol{P}_{ijkl}$ need to be interpolated across the chip. In practice, this can be done by fitting a low-order polynomial to each component separately. Figure 10 shows the PSF ellipticities for the WFPC2 camera derived from globular cluster observations (Figs. 8 and 9), after correction and interpolation.

If the star and galaxy weight functions are equal ($\omega = \omega_*$), then one needs only to keep the first term in equation (54). However, more accurate measurements of the stellar shapes can be achieved by taking a narrower weight function. In addition, it is desirable to avoid recomputing the stellar moments for each value of ω, which is often taken to be a function of the galaxy size. One would then choose $\omega_* < \omega$, making equation (54) converge more slowly than equation (41). In this case, one would thus need to keep the second term in equation (54) and to ensure that the residual error $[O(\rho^6/\omega_*^4)]$ is acceptable compared to that for equation (41) $[O(\rho^4/\omega^2)]$.

5.7. *Special Cases*

Unweighted moments.—In this case, the convolved moments become (eq. [39] with $\omega \to \infty$) $\boldsymbol{J}'_{ij} = \boldsymbol{J}_{ij} + \boldsymbol{P}_{ij}$. Thus, the observed square radius is

$$d'^2 = d^2 + g^2\,, \tag{56}$$

and the observed ellipticity is $\boldsymbol{\epsilon}'_i = (d^2\boldsymbol{\epsilon}_i + g^2\boldsymbol{\epsilon}^p_i)/(d^2 + g^2)$, where g^2 and $\boldsymbol{\epsilon}^p_i$ are defined by equation (42). It is sometimes useful to consider the moments $\boldsymbol{J}^{\rm deconv}_{ij} \equiv \boldsymbol{J}_{ij} - g^2\boldsymbol{\delta}_{ij}$, which have been deconvolved from the isotropic part of the PSF only. The associated radius is $d^{\rm deconv} = d$, while the associated ellipticity is $\boldsymbol{\epsilon}^{\rm deconv}_i = \boldsymbol{\epsilon}_i + (g/d)^2\boldsymbol{\epsilon}^p_i$.

Unweighted moments, circular source.—In this case, $\boldsymbol{\epsilon}_i = 0$, and thus the observed ellipticity becomes

$$\boldsymbol{\epsilon}'_i \equiv \boldsymbol{f}_d\ \boldsymbol{\epsilon}^p_i = \frac{g^2}{d^2 + g^2}\,\boldsymbol{\epsilon}^p_i\,, \tag{57}$$

while the isotropically deconvolved ellipticity becomes

$$\boldsymbol{\epsilon}^{\rm deconv}_i \equiv \boldsymbol{f}^{\rm deconv}_d\,\boldsymbol{\epsilon}^p_i = \left(\frac{g}{d}\right)^2\boldsymbol{\epsilon}^p_i\,. \tag{58}$$

We have introduced the pre- and postdeconvolution reduction factors $\boldsymbol{f}_d$ and $\boldsymbol{f}^{\rm deconv}_d$. These expressions are useful to estimate the effect of the PSF anisotropy on a galaxy.

6. COMBINED EFFECT OF DISTORTION AND CONVOLUTION

In practice, an image is deformed by a series of distortions and convolutions. The full treatment of the combined effect of a distortion and convolution is impractical given the complexity of the $\boldsymbol{D}_{ijkl}$ and $\boldsymbol{C}_{ijkl}$ tensors (eqs. [40] and [22]). However, the general behavior of the ellipticity is captured by considering the simplified case of a circular unweighted source that is subject to a weak distortion. This provides a good model of ellipticities observed in practice (see § 8.3 below).

In the unweighted case [$w(\boldsymbol{\theta}) = 1$] , the normalized quadrupole moments $\boldsymbol{J}'_{ij}$ of an image deformed by a convolution followed by a distortion are (see eqs. [41] and [24] with $\omega \to \infty$)

$$\boldsymbol{J}'_{ij} = (\boldsymbol{J}_{ij} + \boldsymbol{P}_{ij}) + (\boldsymbol{J}_{ik} + \boldsymbol{P}_{ik})\boldsymbol{\phi}_{kj} + (\boldsymbol{J}_{jk} + \boldsymbol{P}_{jk})\boldsymbol{\phi}_{ki} + O(\boldsymbol{\phi}^2) , \tag{59}$$

where $\boldsymbol{P}_{ij}$ are the PSF moments (eq. [38]), $\boldsymbol{\phi}_{ij}$ is the distortion matrix (eq. [18]), and $\boldsymbol{J}_{ij}$ are the undeformed moments. We will assume that the PSF is weakly anisotropic, i.e., that ϵ_i^p defined in equation (42) is small. Then, for an intrinsically circular source ($\boldsymbol{J}_{ij} = d^2\boldsymbol{\delta}_{ij}$), the ellipticity ϵ'_i of the deformed source is

$$\epsilon'_i = \frac{d^2 2\gamma_i + g^2(\epsilon_i^p + 2\gamma_i)}{d^2 + g^2} + O((\boldsymbol{\phi}, \epsilon^p)^2) , \tag{60}$$

where the deformation matrix $\boldsymbol{\phi}_{ij}$ was parametrized as in equation (18), and g is the PSF radius defined in equation (42). Notice that the convergence κ and rotation parameter ρ do not appear in this first order expression. The observed square radius $d'^2 \equiv (J'_{11} + J'_{22})/2$ is given by

$$d'^2 = (1 + 2\kappa)(d^2 + g^2) + O((\boldsymbol{\phi}, \epsilon^p)^2) . \tag{61}$$

For stars ($d = 0$), the observed ellipticity ϵ_i^* becomes

$$\epsilon_i^* = \epsilon_i^p + 2\gamma_i + O((\boldsymbol{\phi}, \epsilon^p)^2) . \tag{62}$$

We can thus rewrite ϵ'_i in terms of observables as

$$\epsilon'_i = \left[1 - \left(\frac{g}{d'}\right)^2\right] 2\gamma_i + \left(\frac{g}{d'}\right)^2 \epsilon_i^* + O((\boldsymbol{\phi}, \epsilon^p)^2) . \tag{63}$$

This expression is useful for computing the expected deformation of objects as a function of their observed size. This simplified model agrees well with the observed deformations in the Survey Strip (see § 8.3).

7. VALIDITY OF THE METHOD

7.1. *Shortcomings*

As was recently pointed out (Kaiser 1999; Kuijken 1999), the KSB method has several shortcomings[2] that limit its validity and accuracy. First, the method requires a decomposition of the PSF into the convolution of an isotropic part and a compact anisotropic part. For most PSFs encountered in practice, this decomposition is formally ill defined and the anisotropic part is not necessarily sufficiently compact. Another problem results from the fact that most PSFs do not fall off fast enough for the second moments (and higher moments) to converge. Consequently, the weighted second moments of the PSF depend strongly on the size of the window function. These problems are particularly severe for the PSF of *HST*, which has broad wings extending beyond a central core, and thus cast doubts on the validity of the numerous weak-lensing analyses based on *HST* observations.

Since our method is based on the same principles as that of the KSB method, it also suffers from the same shortcomings. In addition, we have made the further assumption that, in the decomposition of the PSF, the isotropic part can be taken to be a Gaussian (see § 5.2). This has the advantage of greatly simplifying the deconvolution but can arguably produce further inaccuracies.

These problems are certainly worrisome and might eventually be solved by considering different methods such as those proposed by Kaiser (1999) and Kuijken (1999). However, the KSB approach has the advantage of being relatively simple and of requiring only a small amount of information about the PSF and galaxy shapes, namely, the first few multipole moments. Moreover, these shortcomings are mainly formal in nature. In practice, one indeed always measures moments with a weight function width that is close to the width of the central core of the PSF, and therefore the moments do not diverge. For instance, for the *HST* PSF, the secondary sidelobes that compose the extended wings are smaller in amplitude than the central core by about one order of magnitude. Since the central core dominates in the convolution, one therefore expects that the corrections will be approximately correct. In the following paragraphs, we describe numerical simulations designed to test this assertion quantitatively.

7.2. *Simulations*

To test the weak link in our method, namely, the PSF correction, we performed a series of numerical simulations. We first generated a WFPC2 PSF using the Tiny Tim software (Krist & Hook 1997). We chose the PSF to be particularly noncircular by placing it at the lower right-hand corner of chip 2, at pixel coordinate (100, 100) (see § 8 for a description of the WFPC2 camera and of its PSF). We oversampled the PSF by using pixels that are 10 times smaller than the WFPC2 pixels and did not add any noise to the images. This isolates the systematic deconvolution errors from the random errors produced by pixelization and noise. To maintain uniformity, we will nevertheless quote angular sizes in WFPC2 pixels.

We then measured the weighted moments $\boldsymbol{P}_{ij}$ of the PSF as described in § 5.6, using a range of weight function widths ω_*. For $\omega_* = 2$ pixels, we found the PSF size and ellipticity components (eq. [42]) to be $g \simeq 0.86$ pixels, and $\epsilon_i \simeq \{-0.009, -0.048\}$. As expected, we found both g and ϵ_i to diverge as ω_* increases. For the rest of the simulations, we set $\omega_* = 2$ pixels, which is the stellar weight width that we used in our analysis of the Survey Strip (see § 8.3).

[2] We thank Nick Kaiser, the referee, for pointing out and clarifying these shortcomings.

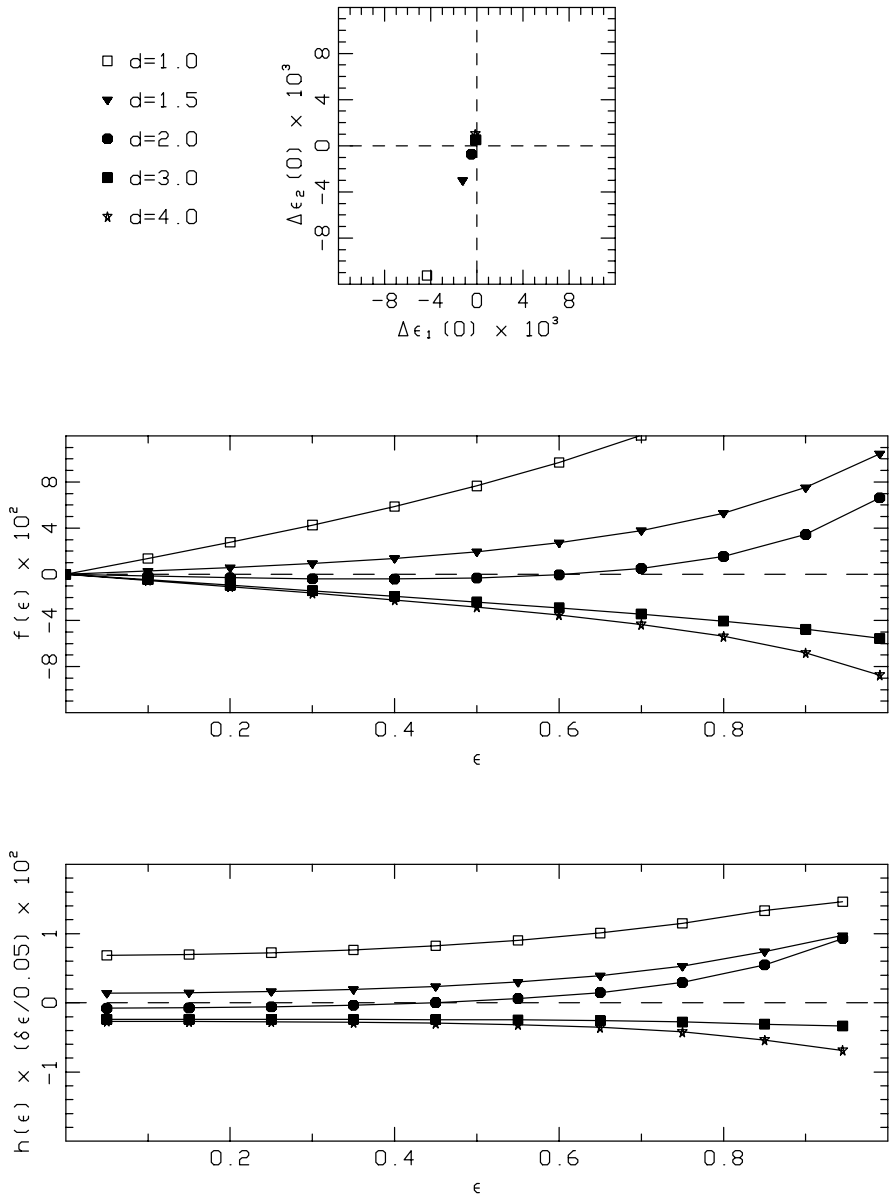

FIG. 2.—Residual errors of the PSF correction determined from numerical simulations. (*Top panel*) The constant term $\Delta\epsilon_i(0)$ and (*middle panel*) the radial function $f(\epsilon)$ for measuring absolute ellipticities. *Bottom panel*: Radial function $h(\epsilon)$ for measuring an ellipticity change of $\delta\epsilon_i = 0.05$ (see text). These quantities are plotted as a function of the unweighted galaxy ellipticity ϵ and size d (in WFPC2 pixels).

We then convolved the PSF with elliptical Gaussian "galaxies" of various intrinsic sizes d and ellipticities ϵ_i. Since the source of the problem lies with the PSF shape, this simplified galaxy model is sufficient for our purposes. We measured the moments of the convolved Gaussian using a weight function width of $\omega = \max(2, d)$ pixels, just as we did for the analysis of the Survey Strip (§ 8.3). We then applied our PSF correction method (§ 5) to obtain the corrected ellipticity $\epsilon_i^{\rm corrected}$, weighted with an effective width ω_g (eq. [47]). For an elliptical Gaussian source, it is easy to show that the true weighted ellipticity is $\epsilon_i^{\rm true} = \epsilon_i[1 + (d/\omega_g)^2(1 - \epsilon^2)]^{-1}$. The error $\Delta\epsilon_i$ induced by the PSF correction on the galaxy ellipticity is thus

$$\Delta\epsilon_i \equiv \epsilon_i^{\rm corrected} - \epsilon_i^{\rm true} \ . \tag{64}$$

We computed this residual error for a range of intrinsic galaxy sizes and ellipticities. The results of these simulations are presented in the next section.

7.3. *Results*

For the range of galaxy shapes that we considered ($1.0 < d < 4.0$ pixels and $\epsilon_i < 1$), we found that, for a given galaxy size d, the ellipticity error $\Delta\epsilon_i$ is very well approximated by

$$\Delta\epsilon_i \simeq \Delta\epsilon_i(0) + f(\epsilon)\hat{\epsilon}_i \ , \tag{65}$$

where $\Delta\epsilon_i(0)$ is a constant, $\hat{\epsilon}_i \equiv \epsilon_i/\epsilon$ is the unit radial ellipticity vector, and $f(\epsilon)$ is a function describing the radial behavior. The constant term $\Delta\epsilon_i(0)$ is shown in the top panel of Figure 2 for several relevant galaxy sizes and has a modulus less than .004 for $d > 1.5$ pixels. The middle panel of Figure 2 shows the radial term $f(\epsilon)$ as a function of the unweighted galaxy ellipticity modulus ϵ, for the same galaxy sizes. The radial term depends strongly on the galaxy size d and ellipticity ϵ and has an amplitude of several percent for moderate ellipticities ($\epsilon < 0.6$) and sizes ($d > 1.5$ pixels). This amplitude is the size of the systematic error made in measuring the ellipticity of a single galaxy.

However, for weak lensing measurements, one is not eventually interested in the ellipticity of a single galaxy, but also in measuring a global change in ellipticity averaged over a galaxy ensemble. Let us consider a change in ellipticity $\epsilon_i \rightarrow \epsilon_i' = \epsilon_i + \delta_i$ produced by lensing[3]. The error in the measurement of $\delta\epsilon_i$ is

$$\Delta\delta\epsilon_i \equiv \langle \Delta\epsilon_i(\epsilon_i') \rangle \simeq \langle \Delta\epsilon_i \rangle + \left\langle \frac{\partial \Delta\epsilon_i}{\partial \epsilon_i} \right\rangle \delta\epsilon_i \,, \tag{66}$$

where the angle brackets refer to the average over the galaxy ensemble. For the functional form of equation (65), this becomes

$$\Delta\delta\epsilon_i \simeq \Delta\epsilon_i(0) + h(\epsilon)\delta\epsilon_i \,, \tag{67}$$

where $h(\epsilon) \equiv \frac{1}{2}[f'(\epsilon) + f(\epsilon)/\epsilon]$. The first term was plotted in the top panel of Figure 2. The second term is shown as a function of ϵ and d in the bottom panel of Figure 2, for an ellipticity change of $\delta\epsilon_i = 0.05$. Since, for our sample $G \simeq 1.4$ (eq. [29]), this value of $\delta\epsilon_i$ corresponds to a shear of $\gamma_i \simeq 0.04$ and is therefore representative of shear signals expected from large-scale structure. For moderate ellipticities ($\epsilon < 0.6$) and sizes ($d > 1.5$ pixels), the second term has an amplitude less than 0.004.

Interestingly, both terms in equation (67) tend to average out, when the distribution of galaxy sizes is considered. Indeed, in our treatment of the Survey Strip (see § 8.4), we selected a sample of "large" galaxies with $d > 1.5$ pixels (and $\epsilon < 1$, which is not always satisfied because of noise). The average size for this sample is $\langle d \rangle \simeq 2.58$ pixels, which is close to the value of d for which both terms change sign (see Fig. 2). The ellipticity dispersion for this sample is $\sigma_\epsilon \simeq 0.31$. Taking $\langle d \rangle$ and σ_ϵ to be representative for this sample, we find the average residual errors to be $\Delta\delta\epsilon_i \approx 0.001$. This cancellation may, however, depend on the galaxy profile, while we have considered only Gaussians in these simulations. To be conservative, we therefore take the residual error for our sample to be about 0.004, which is the error before averaging over d values. This is close to the residual error estimated from the anisotropic correction of the stars in our analysis of globular cluster fields (§ 8.4).

We also studied how the choice of the weight function widths ω and ω_* affect these results. We found that for moderate values ($1 < \omega_* < 3$ and $0.5d < \omega < 2d$), the magnitude of the residual errors did not change significantly from the above. However, the errors were much larger for ω and ω_* outside of these ranges. This is, of course, a consequence of the divergences present in the PSF moments.

We conclude that, the ellipticity error produced by the PSF correction can be several percent for an individual galaxy observed with WFPC2. However, it is only about 0.004 when averaged over a galaxy ensemble with $d > 1.5$ pixels, provided moderate values of the weight function widths are used. This does not alleviate the serious formal shortcomings of the method, and the need for a search for more robust methods (see Kaiser 1999; Kuijken 1999).

8. APPLICATION TO *HST* IMAGES

As an application of our method, we consider weak-lensing measurements with the WFPC2 camera on board *HST*. The camera consists of three 800 × 800 pixel chips, with a pixel size of 0.″1. With the F814W filter, the PSF has a FWHM of about 0.″09. The instrumental effects for WFPC2 have been studied in detail by HFKS. They showed that the two main systematic effects for this instrument are the camera distortion and the PSF. We repeat their analysis by considering each of these effects in turn. We then apply these results to the galaxies found in the Survey Strip.

8.1. *Camera Distortion*

The camera distortion is caused mainly by the field flattener, a refractive element in the WFPC2. This effect has been studied by Holtzman et al. (1995), who quantified this effect using astrometric measurements of globular cluster observations. They modeled the distortion by a cubic polynomial in chip position for each chip. The polynomial coefficients can be used to derive a transformation matrix $\phi_{ij}^{\rm camera}$ between the WFPC2 chip coordinates (which are the distorted coordinates x' in eq. [16]) and the undistorted coordinates (x in the same equation).

The distortion field is shown in Figure 3. The quantity plotted is $\epsilon_i^\phi \equiv 2\gamma_i$, the ellipticity induced by the distortion field ϕ_{ij} on an intrinsically circular source (see eq. [33]). The pattern is radial and increases in magnitude with distance from the chip center. This differs from the results of HFKS who derived a tangential rather than radial camera distortion field. The radial nature of the pattern is confirmed by the fact that, using the coefficients of Holtzman et al. (1995) in equation (35), we find $(df/dx - f/x) > 0$. (This can also be confirmed by drawing a box connecting the heads and tails of four adjacent arrows in Fig. 15 in Holtzman et al.) To study the profile of the ellipticity pattern, it is useful to define the rotated ellipticity by

$$\epsilon_i^r \equiv R_{ij}(-2\varphi)\epsilon_j \,, \tag{68}$$

where ϵ_i is the ellipticity of an object in the chip frame, R_{ij} is the rotation matrix defined in equation (7), and φ is the polar

[3] Strictly speaking, the ellipticity change δ_i produced by weak lensing has a weak dependence on ϵ_i (see eq. [31]). While this effect is important only for large ellipticities, the ensemble average is dominated by small ellipticities. For the purpose of estimating the size of the average correction error, we can thus ignore this small effect and consider a constant ellipticity shift.

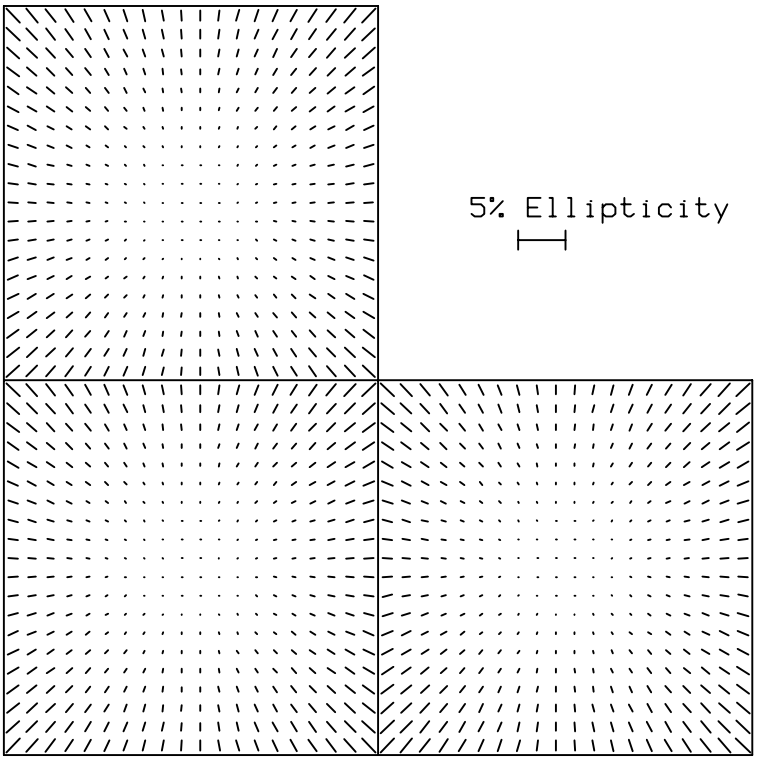

FIG. 3.—WFPC2 detector shear pattern. The quantity plotted is $\epsilon_i^{\phi} = 2\gamma_i$, which is the ellipticity induced by the detector shear for an intrinsically circular source. Chips 2, 3, and 4 are in the upper left, lower left, and lower right corners, respectively. Chip 1 (the planetary camera) is not shown. Each chip is 1.3 on a side.

angle of the source position about the center of the chip, measured counterclockwise from the x-axis. A positive (negative) value of ϵ_1^r corresponds to a radial (tangential) ellipticity pattern. A positive (negative) value of ϵ_2^r corresponds to an anticlockwise (clockwise) swirl pattern. The meaning of ϵ_i^r is illustrated in Figure 4.

The profile of the rotated distortion ellipticity is shown as the dot-dashed line on Figure 5. The mean ellipticity averaged over the three chips is listed in Table 1. The mean rotated ellipticities are found to be $\langle \epsilon_1^r \rangle \simeq 0.007$ and $\langle \epsilon_2^r \rangle < 0.001$, while the mean absolute ellipticity $\langle \epsilon_i \rangle$ is less than 0.001. The effect of the camera distortion is thus small but nevertheless comparable to the lensing signal expected from large-scale structure.

8.2. *Point-Spread Function*

The PSF is affected by diffraction by the telescope and scattering of light from different parts of the telescope and the optics. The PSF depends both on wavelength and time. The time dependence has two components (Krist & Hook 1997). The first one is due to orbit-to-orbit "breathing" of the telescope. As the telescope orbits the earth every 90 minutes, it passes into and out of sunlight. The heating and cooling of the telescope changes its size, and thus its focus and PSF. The second time-dependent factor arises from a change in the focus of the telescope over longer periods of time. This change is produced by the outgassing of the graphite epoxy truss that supports the primary mirror. Approximately every 6 months, the secondary mirror is moved to bring the telescope back into optimal focus. The time dependence of the focus position is summarized in Figure 6.

8.2.1. *Tiny Tim*

As a first step, we used the Tiny Tim software to model the PSF of the *HST* (Krist & Hook 1997). Tiny Tim takes into account the diffraction of light by the telescope to create a PSF, given the instrument (WFPC2 in our case), chip number, chip position, filter, spectrum of the object being modeled, and the focus of the telescope. Tiny Tim does not include the geometric distortion discussed above.

We used Tiny Tim to model the PSF across the three WFPC2 chips. We chose the F814W filter and the spectrum of the objects to be similar to that of a type G star ($B-V = 0.619$), which is typical of galaxies in the Survey Strip (see § 8.3). We measured the moments (eq. [5]) and weighted them with a circular Gaussian (eq. [3]). For all stellar measurements, we adopted a weight-function width of $\omega_* = 2$ pixels, which resulted in an optimal sensitivity.

To study the variation of the PSF across the chip, we used Tiny Tim to create a grid of PSFs. These PSFs were generated for a telescope with a mirror at a focus position of -1.5 μm, the value of the focus when the Survey Strip was taken (see § 8.3). The resulting ellipticity pattern is shown in Figure 7. The corresponding ellipticity profile averaged over all chips is shown as the central dashed line in Figure 5. In these figures, we have added the effects of the detector shear shown in Figure 3 so that a direct comparison can be made between these simulations and the globular cluster measurements, which are presented below.

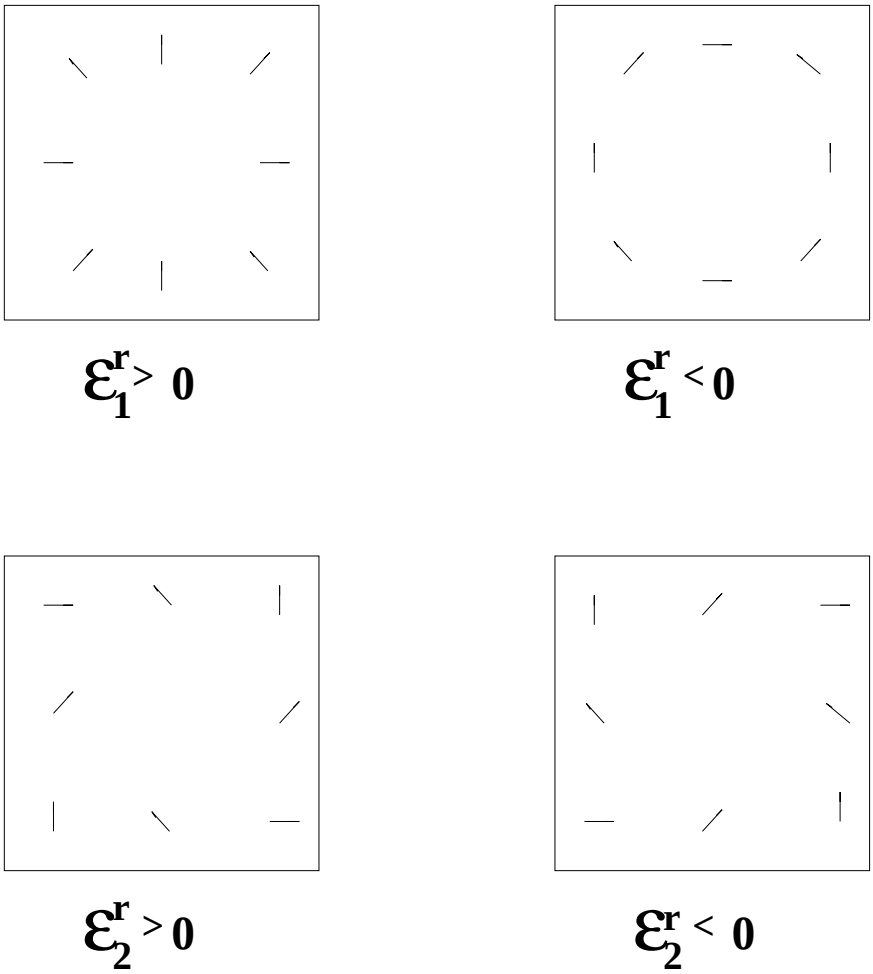

FIG. 4.—Illustration of the meaning of rotated ellipticity ϵ_i^r. This ellipticity is defined by choosing coordinates axes that are rotated about the chip center. The patterns corresponding to positive and negative values for each component of ϵ_i^r are shown.

TABLE 1

EFFECT OF CORRECTIONS ON CHIP-AVERAGED ELLIPTICITIES

Sample	Corrections[a]	$\langle\epsilon_1^r\rangle$	$\langle\epsilon_2^r\rangle$	$\langle\epsilon_1\rangle$	$\langle\epsilon_2\rangle$	σ_ϵ[b]
Camera distortion		0.007 ± 0.001	−0.000 ± 0.001	0.000 ± 0.001	−0.000 ± 0.001	
M4 + NGC 6572		−0.047 ± 0.001	0.001 ± 0.001	−0.014 ± 0.001	−0.020 ± 0.002	
	d, a	−0.003 ± 0.001	0.000 ± 0.001	−0.002 ± 0.001	0.002 ± 0.001	
M4		−0.040 ± 0.002	−0.001 ± 0.001	−0.010 ± 0.001	−0.020 ± 0.002	
	d, a	0.004 ± 0.001	0.000 ± 0.001	0.003 ± 0.001	0.003 ± 0.001	
NGC 6572.....		−0.053 ± 0.002	0.003 ± 0.002	−0.019 ± 0.002	−0.020 ± 0.003	
	d, a	−0.009 ± 0.001	−0.000 ± 0.001	−0.007 ± 0.001	0.001 ± 0.001	
Tiny Tim[c] (-1.5μ).....		−0.035 ± 0.003	−0.000 ± 0.003	−0.032 ± 0.002	−0.031 ± 0.003	
($+2.0\mu$).....		−0.033 ± 0.003	−0.001 ± 0.002	−0.025 ± 0.001	−0.023 ± 0.003	
(-5.0μ).....		−0.038 ± 0.004	−0.000 ± 0.003	−0.038 ± 0.002	−0.037 ± 0.004	
Small galaxies[d].....		−0.009 ± 0.004	−0.002 ± 0.004	0.005 ± 0.004	−0.005 ± 0.004	0.24
	d	−0.013 ± 0.004	−0.001 ± 0.004	0.004 ± 0.004	−0.004 ± 0.004	0.24
	d, a	0.004 ± 0.004	0.000 ± 0.004	0.011 ± 0.004	0.005 ± 0.004	0.24
Large galaxies[d].....		0.004 ± 0.003	−0.000 ± 0.003	0.006 ± 0.003	−0.005 ± 0.003	0.24
	d	0.001 ± 0.003	−0.000 ± 0.003	0.007 ± 0.003	−0.006 ± 0.003	0.24
	d, a	0.005 ± 0.003	0.000 ± 0.003	0.009 ± 0.003	−0.003 ± 0.003	0.24
	d, a, i	0.008 ± 0.004	−0.000 ± 0.004	0.009 ± 0.004	−0.001 ± 0.004	0.31

[a] Corrections: d = camera distortion, a = PSF anisotropy, and i = isotropic PSF. The PSF is derived from the combined M4 and NGC 6572 stars.

[b] $\sigma_\epsilon^2 \equiv \frac{1}{2}\langle\epsilon^2\rangle = \frac{1}{2}(\langle\epsilon_1^2\rangle + \langle\epsilon_2^2\rangle)$.

[c] PSF predicted by Tiny Tim for several focus values.

[d] Galaxies with magnitudes $I < 26$, ellipticities $\epsilon < 1$, and observed radii $1.0 < d' < 1.5$ and $d' > 1.5$ pixels, for the small and large samples, respectively.

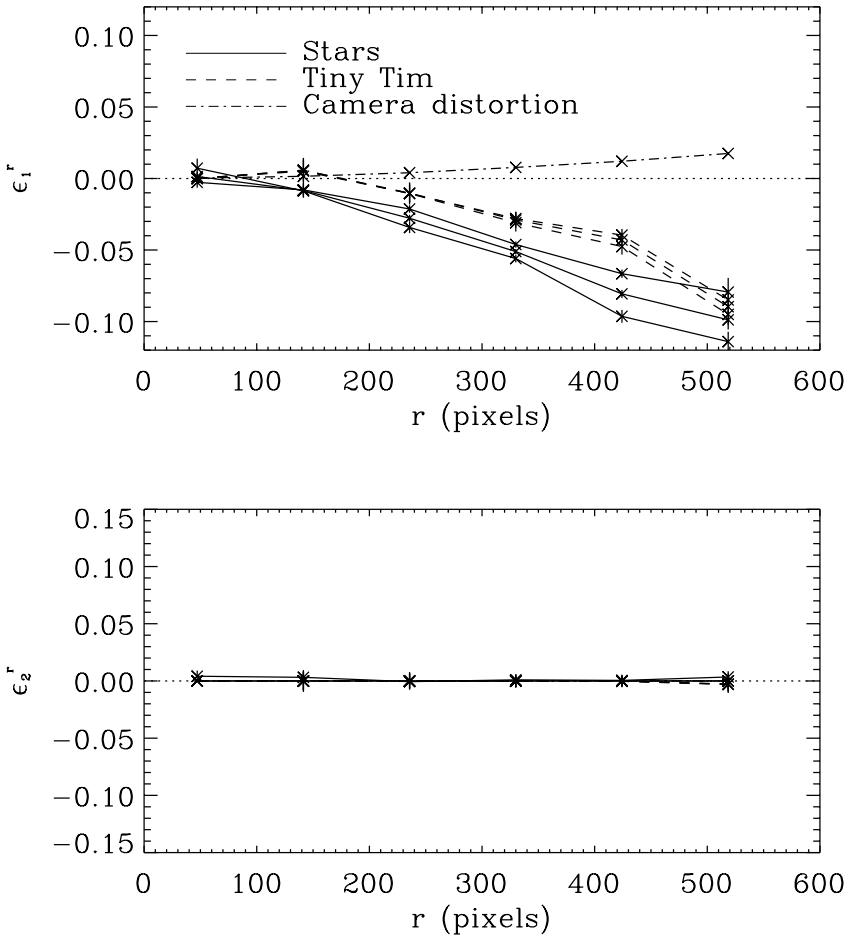

FIG. 5.—Rotated ellipticity profile for the PSF and the camera distortion, as a function of radius about the chip center. The solid lines show the ellipticity as measured for M4, combined M4/NGC 6572 , and NGC 6572 stars, from top to bottom, respectively. The dashed lines show the PSF ellipticity predicted by Tiny Tim for focus values of +2.0, −1.5, and −5.0 μm, from top to bottom, respectively. The dot-dashed line shows the distortion ellipticity ϵ_i^ϕ.

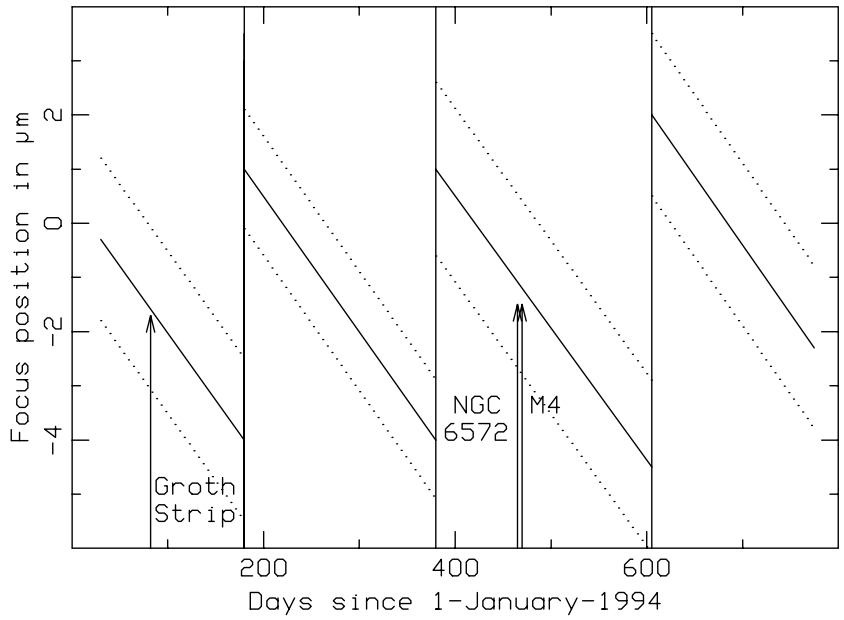

FIG. 6.—*HST* focus as a function of time. The vertical lines give the times of mirror movements generated to bring the telescope back into focus. The diagonal lines represent the average mirror position as a function of time. Orbit-to-orbit "breathing" produces considerable variations (up to several microns) about these mean values. The rms value of these variations is shown by the dotted lines. This figure is patterned after Fig. 5.7 in Biretta (1996). The values corresponding to the observations of the Survey Strip and of the M4 and NGC 6572 globular clusters are also indicated.

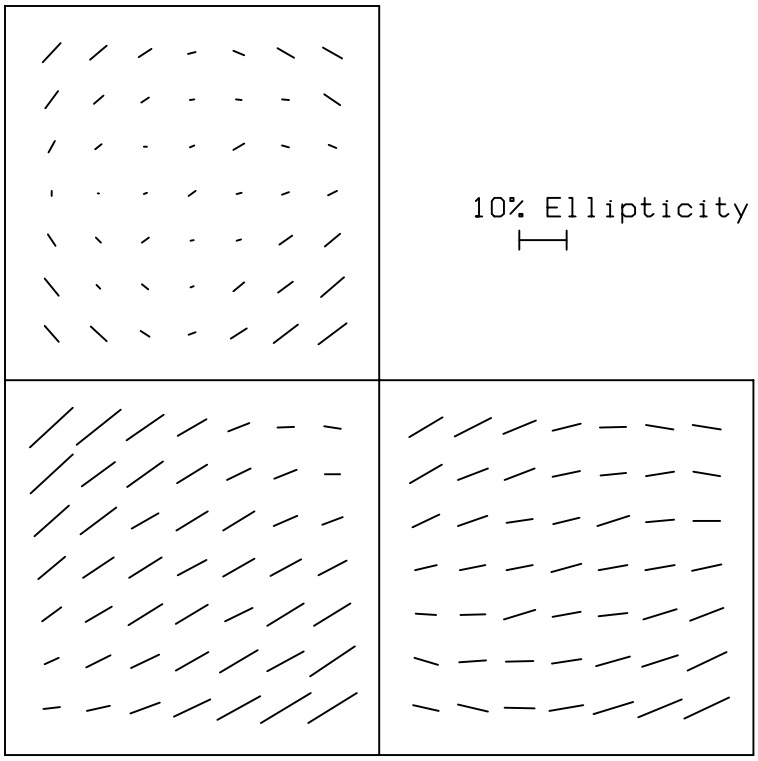

FIG. 7.—PSF ellipticity predicted by Tiny Tim. This figure corresponds to a focus of -1.5 μm, close to the mean value for the Survey Strip observations. The ellipticities are shown after application of the camera distortion.

The predicted PSF anisotropy is quite large ($\langle \epsilon_1^r \rangle \simeq 0.1$ at the edge) and varies significantly across each chip and from chip to chip.

To test the effect of focus changes, we created Tiny Tim PSFs at focus values of $+2.0$ μm and -5.0 μm, the full range of telescope focus (see Fig. 6). The ellipticity profiles are shown are the upper and lower dashed curves in Figure 5. The chip-averaged ellipticities for each focus value are listed in Table 1. Extreme focus changes from the central value of -1.5 μm produce variations of about 0.002 for $\langle \epsilon_1^r \rangle$ and about 0.006 for $\langle \epsilon_1 \rangle$ and $\langle \epsilon_2 \rangle$, when averaged over all chips.

8.2.2. *Globular Clusters*

For a more direct measurement of the PSF, we obtained archival images of the globular cluster M4 observed by Richer et al. (1997). We also obtained archival images of the globular cluster NGC 6572. This was the method of calibration used by HFKS. It is fortuitous that the M4, NGC 6572, and Survey Strip data all have focus values of approximately -1.5 μm (see Fig. 6).

The M4 data consisted of three different fields in each cluster. Each field had eight different exposures: four pairs of dithered pointings separated by very nearly 2 pixels. Other dithers were separated by noninteger numbers of pixels. We shifted the dithers that are separated by integer numbers of pixels and compared them pairwise to detect cosmic rays. A pixel was flagged as a cosmic ray if its flux was significantly above that of the corresponding pixel in its pair image. We selected stars from the M4 exposures by excluding saturated stars and those that are faint and dominated by noise. We also excluded stars confused by close neighbors and stars containing a cosmic-ray–flagged pixel within a 5 pixel radius. Our resulting sample consisted of about 160 stars per chip. We then averaged the three moments $\boldsymbol{P}_{kl}$ measured in each of the eight exposures. The analysis of the NGC 6572 data was simplified by the fact that we had only one field and the images were not dithered.

The ellipticity fields for M4 and NGC 6572 are shown in Figures 8 and 9, respectively. The ellipticity profile for each globular cluster is shown as the upper and lower solid line in Figure 5, respectively. The chip-averaged ellipticities for each globular cluster data set are listed in Table 1. The M4 and NGC 6572 ellipticity patterns are qualitatively similar, and both show tangential ellipticities of the order of 0.1 at the edge of all chips. The M4 and NGC 6572 average ellipticities $\langle \epsilon_1^r \rangle$ are -0.040 and -0.053, respectively, and are both larger than that predicted by Tiny Tim (about -0.035). The fact that the mean tangential ellipticity for NGC 6572 is larger than that for M4 by about 0.013, shows that the PSF varies substantially over periods as short as a few days. This change is larger than that predicted by Tiny Tim for extreme focus changes (see § 8.2.1). Moreover, the globular cluster ellipticities are qualitatively different from that predicted by Tiny Tim. For example, Figure 10 shows a "teardrop" shape to the M4 ellipticity pattern of chip 2, with a cusp at the top of the chip. In contrast, the Tiny Tim ellipticity pattern of the same chip, shown in Figure 7, has a cusp on the right-hand side. Small changes in this cusp result from changing the focus of the telescope in Tiny Tim, but these do not change the qualitative pattern of the ellipticities.

Because of these shortcomings, we used the observed globular cluster moments for the corrections, rather than the Tiny Tim predictions. To reduce patchiness, we combined the M4 and NGC 6572 stars, and corrected the moments for the weight function (eqs. [54] and [55]) and for the camera distortion (eqs. [24] and [25] with $\omega \to \infty$) to obtain the PSF moments $\boldsymbol{P}_{ij}$

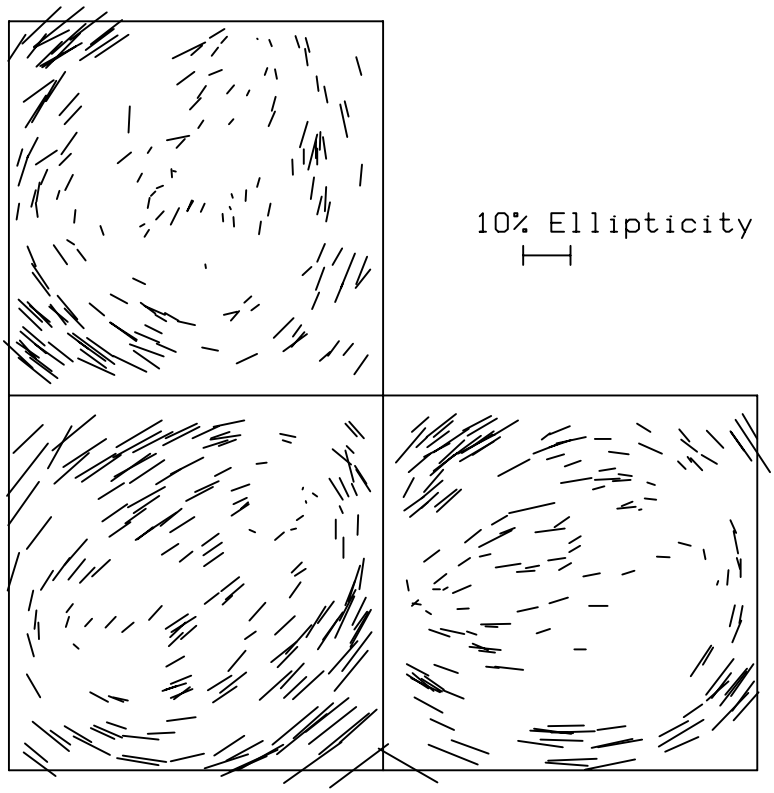

FIG. 8.—Ellipticities of the stars in the globular cluster M4. A Gaussian weight function of width $\omega_* = 2$ pixels was used to measure the stellar moments.

and $\boldsymbol{P}_{ijkl}$. We then fitted a fifth-order polynomial in chip position for each moment component and for each chip. Because the star counts in the two globular cluster are close to one another (i.e., about 160 per chip), this amounts to giving equal weight to each of them. The ellipticity profile for the combined globular clusters is shown as the central solid line in Figure 5. Figure 10 shows the resulting fitted ellipticity pattern of the PSF.

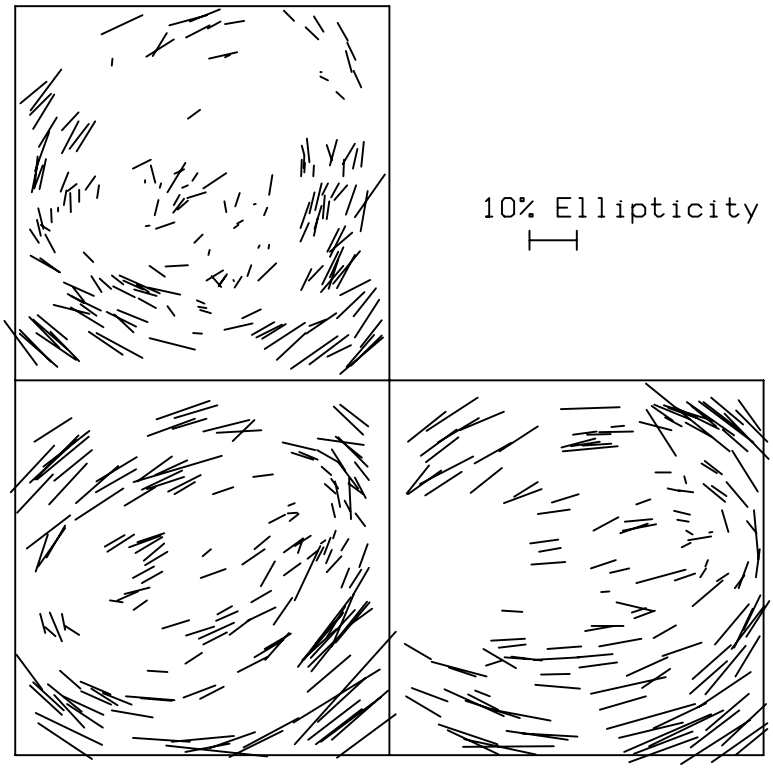

FIG. 9.—Ellipticities of the stars in the globular cluster NGC 6572

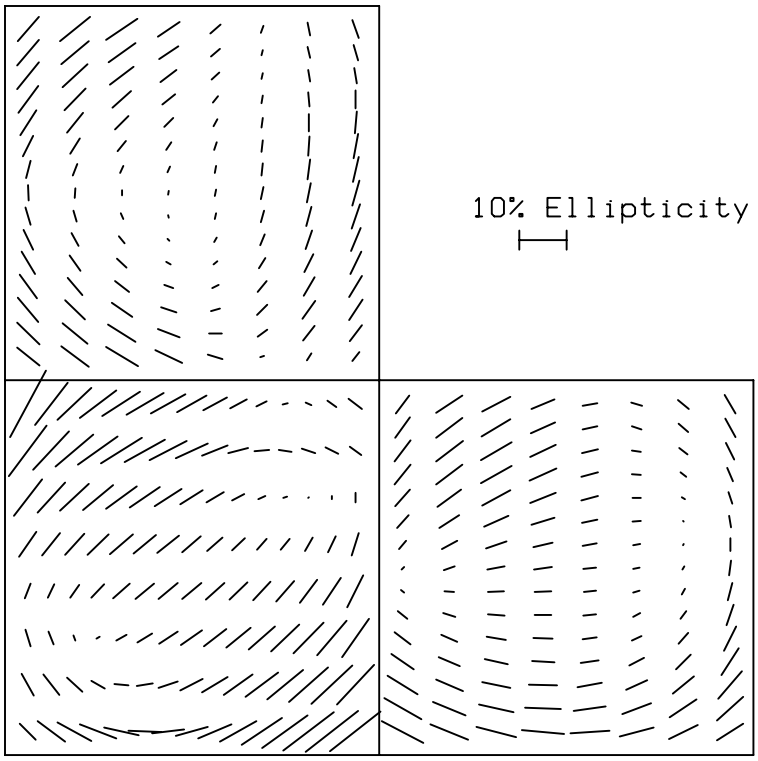

FIG. 10.—PSF ellipticities derived from the combined M4/NGC 6572 stars after being corrected for shear and weighting and interpolated

The mean PSF radius for the combined M4/NGC 6572 was found to be $g \simeq 0.89$ pixels (see eq. [42]). This is much smaller than the formal PSF radius that one would measure using a Tiny Tim PSF with $\omega_* \to \infty$. As explained in § 7.1, the quadrupole moments indeed formally diverge because of the extended wings of the *HST* PSF. Our value is however commensurate with the PSF FWHM (0.9 pixels), and should thus be considered as an effective PSF radius.

8.3. *Survey Strip*

The Survey Strip is a set of 28 contiguous pointings with the *HST* in two colors, *V* (F606W) and *I* (F814W) (Groth et al. 1994; Rhodes 1999). The images were taken in 1994 March and April with the WFPC2. The Strip has about 10,000 galaxies down to $I \approx 26$ and covers an area of about 108 arcmin^2 over a $3'.5 \times 44'.0$ region. The Strip has already proved a useful data set in exploring the distribution of luminous matter through number counts and the two-point angular correlation function (Rhodes et al. 1997; Rhodes 1999). We are in the process of exploring the large-scale distribution of matter through weak lensing of the Strip galaxies (Rhodes 1999; Rhodes, Refregier, & Groth 2000, in preparation).

Here, we use the Strip galaxies to test our shear measurement method. For this purpose, we used the *I* images only. The catalog of galaxies was created using the Faint Object Classification and Analysis System (FOCAS) within IRAF (Jarvis & Tyson 1981). An object was considered as detected if two contiguous pixels were more than 3 σ above the sky background. However, an object was included in the final catalog only if both the *I* and *V* images had detections within an error box of approximately 5 pixels ($0''.5$). This resulted in a sample of 9448 galaxies with $I < 26$.

The moments of the galaxies were calculated as described above (eq. [5]). The variable weight function was chosen to be $\omega = \max [2, (A/\pi)^{1/2}]$, where A is the detection area calculated by FOCAS. The lower bound of ω was chosen to match the width ω_* used for stars. The importance of the camera distortion and of the PSF depends on the radius d of the galaxy (eq. [11]). We thus considered subsamples of small and large galaxies, with $1.0 < d' < 1.5$ pixels and $d' > 1.2$ pixels, respectively. Here d' is the rms observed radius (eq. [56]) and $g \simeq 0.89$ pixels is the PSF radius (see § 8.2.2). Because of the noise, a fraction of the galaxies have unphysical ellipticity values ($\epsilon > 1$). Because these outliers would dominate ellipticity statistics, we retained only galaxies with $\epsilon < 1$. The mean observed radius and reduction factor (eq. [57]) are $\langle d' \rangle \simeq 1.26$ pixels and $f_d \simeq 0.50$, and $\langle d' \rangle \simeq 2.16$ pixels and $f_d \simeq 0.17$, for the small and large galaxies, respectively. Each subsample respectively comprises 41% and 77% of the total number of $I < 26$ galaxies.

The ellipticity profile for each subsample is shown as a solid line in Figures 11 and 12. Also shown are the asymptotic cases, namely, the combined M4/NGC 6572 stars ($d = 0$) and the camera distortion ellipticity ($d \to \infty$). The dashed line shows the prediction of the simplified model described in § 6 (see eq. [63]). The small galaxy sample shows a tangential ellipticity that increases with radius from the chip center, in agreement with the model prediction. The large galaxies, on the other hand, do not display any significant tangential ellipticity, again in agreement with the model. In both cases, $\langle \epsilon_2^r \rangle$ is consistent with zero.

Using the camera distortion matrix derived in § 8.1 and the PSF moments derived in § 8.2, we then corrected the Strip galaxies. The ellipticity profiles at different stages of the correction for the small and large galaxy subsamples are shown in Figures 13 and 14. Since the camera distortion is radial, its correction increases the tangential ellipticity of the galaxies. On the

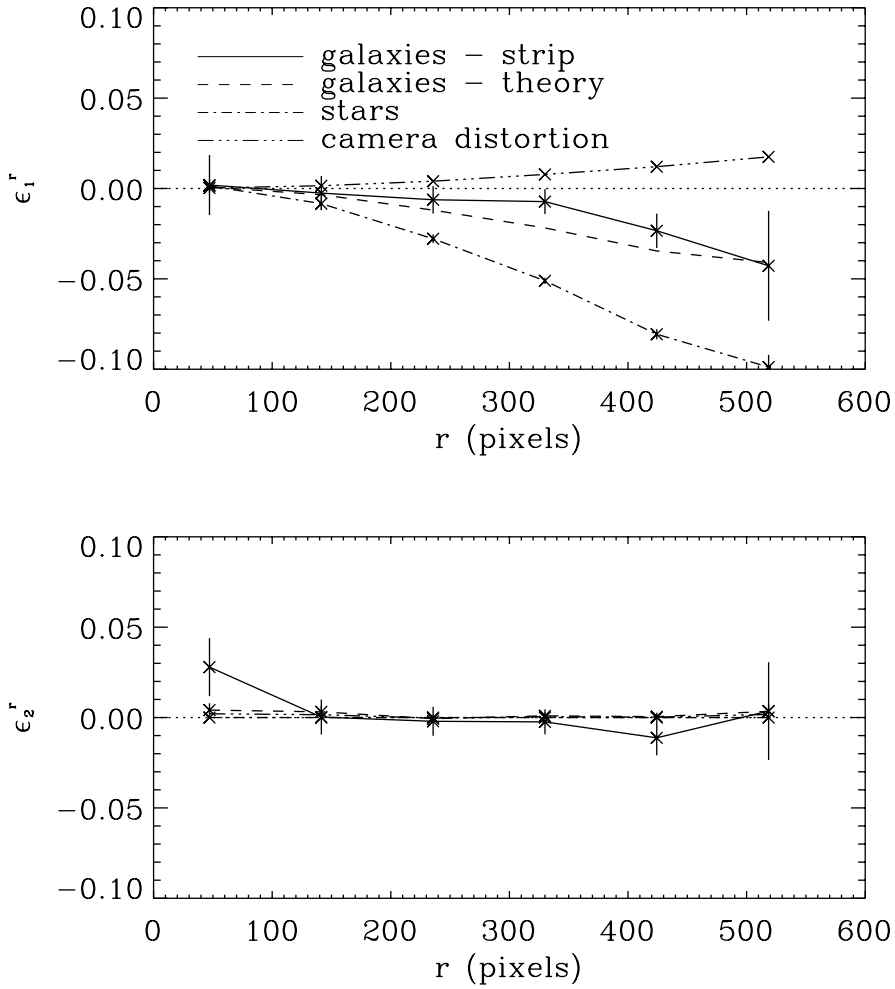

FIG. 11.—Rotated ellipticity profile for small galaxies in the Survey Strip. Galaxies were selected to have $I < 26$ and radii $1.0 < d' < 1.5$ pixels. The PSF and the camera distortion ellipticity $\epsilon_i^{\phi,r}$ are also shown for comparison. The profile for the Strip galaxies expected in the simplified theoretical model is also shown (see text).

other hand, the correction for the PSF, which is mainly tangential, reduces the tangential component of the ellipticity. For both subsamples, the resulting corrected profile is consistent with 0. As expected, the PSF correction has a smaller effect on the large galaxies than on the small galaxies.

8.4. *Error Budget*

The effect of the corrections for the chip-averaged ellipticities are summarized in Table 1. To ensure statistical independence, we considered in this table a subsample of large galaxies with $d' > 1.5$ pixels (and $\epsilon < 1$). This subsample contains 51% of the total number of galaxies with $I < 26$, corresponding to a surface density of $n \simeq 32$ arcmin^{-2}. Their mean observed radius is $\langle d' \rangle \simeq 2.58$ pixels, corresponding to a postdeconvolution reduction factor of $f_d^{\rm deconv} \simeq 0.13$ (eq. [58]). As a test of the correction algorithm, we also corrected the globular cluster stars, exactly as we corrected the galaxies. (We have not corrected either the stars or the small galaxies for the isotropic PSF, as this would produce diverging ellipticities.) The results for the corrected stars are also shown in the table.

The self-corrected M4/NGC 6572 stars have residual ellipticities of $\langle \epsilon_1^r \rangle \simeq 0.003$ and $\langle \epsilon_1 \rangle \simeq \langle \epsilon_2 \rangle \simeq 0.002$. This is a measure of the errors resulting from the approximations in our correction method and from the fit to the stellar moments. Another estimation of the errors from the method was presented in § 7. By performing numerical simulations, we showed that the residual ellipticity errors in the PSF correction was 0.004, after averaging over a galaxy ensemble with $d > 1.5$ pixels. Given the agreement of these two estimates, we take the error in the correction method to be about 0.004.

As we noted in § 8.2, the M4 and NGC 6572 ellipticities differ by about 0.01 for both rotated and absolute ellipticities. After the anisotropic PSF correction, the small galaxies have a residual ellipticity of $\langle \epsilon_1^r \rangle \simeq 0.004$, $\langle \epsilon_2 \rangle \simeq 0.011$ and $\langle \epsilon_1 \rangle \simeq 0.005$. Since the small galaxies have a reduction factor of $f_d \simeq 0.50$, their residual $\langle \epsilon_1 \rangle$ ellipticity indicates that the PSF variation is about 0.02, which is larger than that given by the comparison of M4/NGC 6572. We therefore take the variations of the chip-averaged PSF ellipticity to be about 0.02.

How does this uncertainty affect the ellipticities of the large galaxies? As noted above, the postdeconvolution reduction factor for the large galaxies (with $d' > 1.5$ pixels) is $f_d^{\rm deconv} \simeq 0.13$. Consequently, our uncertainty of 0.02 in the PSF ellipticity produces an uncertainty in the ellipticities of the large galaxies of only 0.003. This is of course a commendable consequence of

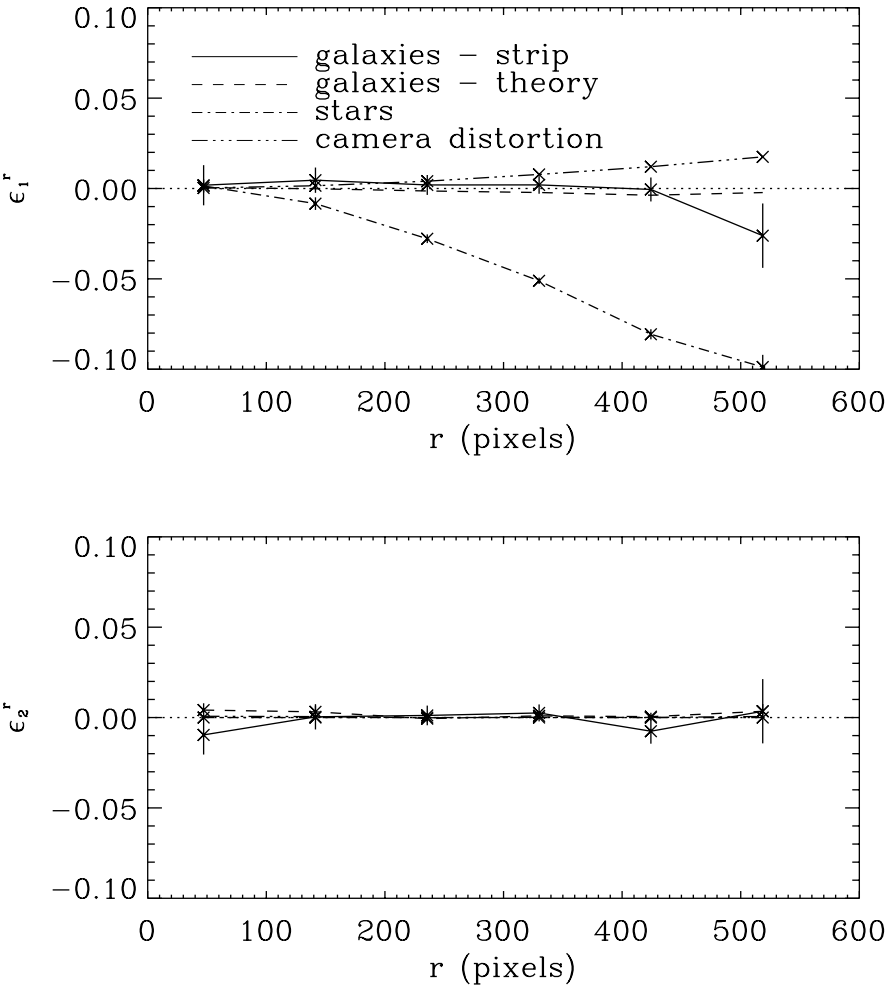

FIG. 12.—Same as the previous figure, but for large galaxies ($d' > 1.2$ pixels)

the small size of the WFPC2 PSF. Note also that, for the large galaxies, the camera distortion correction is about the same size as that for the PSF, so that the two corrections almost cancel each other. The changes in ellipticities produced by each of these corrections is less than 0.005 for the large galaxies. The total systematic uncertainty is a combination of the correction uncertainty and of the PSF variability and is thus about 0.004.

The statistical uncertainties are determined by the ellipticity variance $\sigma_\epsilon^2 \equiv \frac{1}{2}\langle \epsilon^2 \rangle = \frac{1}{2}(\langle \epsilon_1^2 \rangle + \langle \epsilon_2^2 \rangle)$. Both noise in the image and the intrinsic shapes of the galaxies contribute to this dispersion. The rms ellipticity σ_ϵ is listed in the last column of Table 1, at various stages of the correction. For both the large and small galaxies, σ_ϵ does not increase when we correct for the camera distortion and for the anisotropic PSF. This shows that our correction method does not introduce any appreciable noise in the ellipticity measurements. Not surprisingly, σ_ϵ increases moderately when we correct for the isotropic PSF. This is expected since this deconvolution reduces the galaxy size and thus reduces the denominator in the definition of the ellipticity. For the large galaxies, the rms ellipticity after all corrections is about $\sigma_\epsilon \simeq 0.31$. Since the mean number of such galaxies per chip is about $N_g \simeq 57$, the 1 σ sensitivity to detect the shear in a chip is $\sigma_\epsilon/(N_g)^{1/2} \simeq 0.04$. This is close to the expected rms shear expected from weak lensing by large-scale structure in 1.′3 cells for cluster normalized cold dark matter (CDM) models and for a source redshift $z = 1$ (Jain & Seljak 1997). This shows that the expected signal-to-noise ratio of a single WFPC2 chip is about 1.

9. CONCLUSIONS

We have revisited the KSB method to measure the weak lensing shear from the shapes of galaxies. In our method, the corrections for the camera distortion and PSF convolution are performed using moments rather than ellipticities. Using a Gaussian weight function, we derived explicit expressions for the corrections, which involve only second- and fourth-order moments. We clarified the convergence of some of the approximations made by KSB and showed how the weight function for stars can be chosen to be different from that for galaxies. We also showed how the isotropic part of the PSF can be assumed to be a Gaussian, to the required level of precision, and can thus be corrected for exactly. We derived the explicit relation between the shear and the ellipticities by decomposing moments into tensors with definite rotational properties.

We addressed the recently exposed shortcomings of the KSB method (Kaiser 1999; Kuijken 1999). Our method, as well as the KSB method, has formal problems arising from the fact that PSFs encountered in practice are not sufficiently compact.

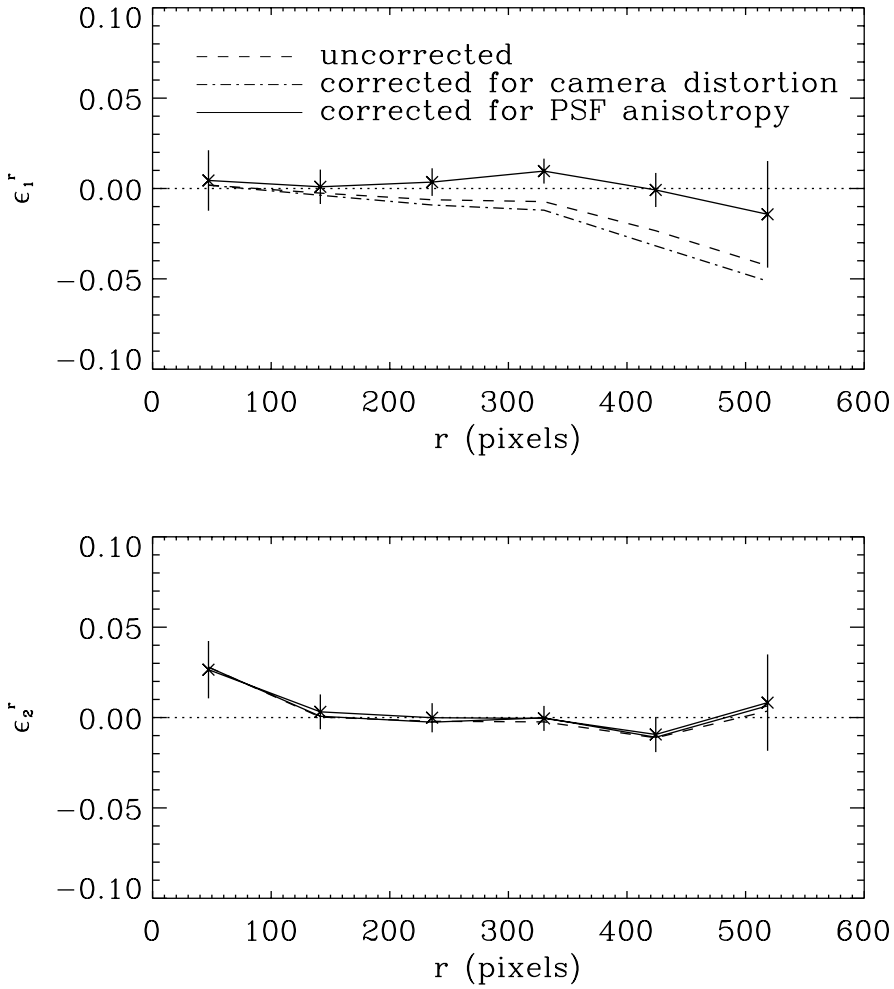

FIG. 13.—Effect of the corrections for small galaxies ($1.0 < d' < 1.5$ pixels, $I < 26$) in the Survey Strip. The profile for the galaxies is shown at different stages of the correction algorithm. The error bars are similar for each of the three profiles, but, for clarity, were displayed only for the last case.

We used numerical simulations to assess the importance of these problems in the analysis of WFPC2 images. We found that the ellipticity error produced by the PSF correction can be several percent for an individual galaxy. However, it is only about 0.004 when averaged over a galaxy ensemble with $d > 1.5$ pixels, provided moderate weight function widths are used.

We studied systematic effects arising in WFPC2 images. From globular cluster observations, we confirm the results of HFKS, who found $\sim$10% PSF ellipticities at the edge of each chip. We find however that the camera distortion is radial rather than tangential. It produces ellipticities of the order of 0.7%. We further find that the PSF ellipticity varies by as much as 2% over time.

We applied our correction method to the *HST* Survey Strip. We showed that the different stages of our correction do not introduce any appreciable noise. We studied the dependence of galaxy ellipticities on the galaxy size. Small galaxies are more sensitive to the PSF and also indicate that the PSF varies with time. For large galaxies (observed radii $d' > 1.5$ pixels), the total systematic uncertainty is about 0.4% and results from a nearly equal contribution from the correction uncertainty and from the PSF variability. The statistical 1 σ uncertainty in measuring the shear in a single WFPC2 $1\farcm3 \times 1\farcm3$ chip is about 4% for this subsample of galaxies. This provides good prospects for detecting a cosmic shear signal with the Strip and other deep *HST* surveys. In Rhodes, Refregier, & Groth (2000, in preparation) and Rhodes (1999), we will describe our search for such a signal.

We thank Richard Ellis, Peter Schneider, Stella Seitz, Henk Hoekstra, Christophe Alard, David Bacon, and Meghan Gray for useful discussions. We are grateful to Nick Kaiser, the referee, for insightful comments and criticisms. A. R. was supported by the NASA MAP/MIDEX program and by the NASA ATP grant NAG5-7154. E. G. and J. R. were supported by NASA grant NAG5-6279 and would like to thank the WFPC1 IDT for cooperation on this project.

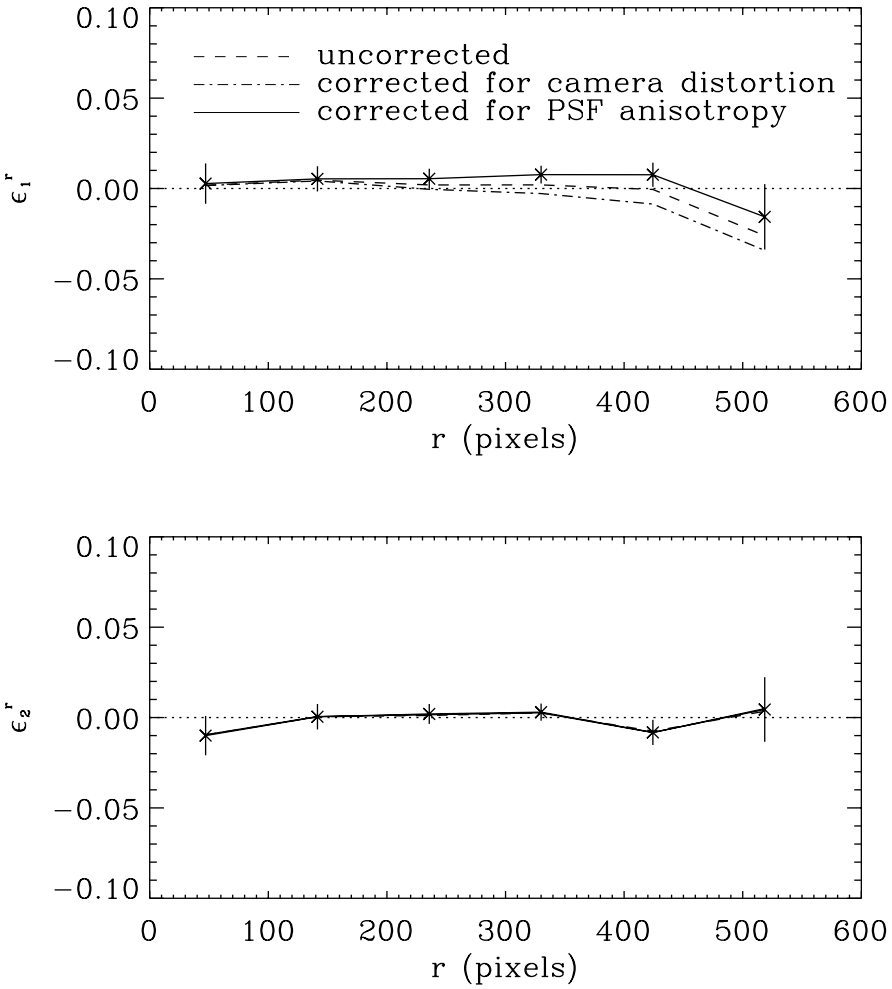

FIG. 14.—Same as the previous figure, but for large galaxies ($d' > 1.2$ pixels)

REFERENCES

Biretta, J. 1996, The WFPC2 Instrument Handbook (Baltimore: STScI)
Bonnet, H., & Mellier, Y. 1995, A&A, 303, 331
Fort, B., & Mellier, Y. 1994, A&A Rev., 5, 239
Groth, E. J., et al. 1994, BAAS, 26, 1403
Hoekstra, H., Franx, M., Kuijken, K., & Squires, G. 1998, ApJ, 504, 636 (HFKS)
Holtzman, J. A., et al. 1995, PASP, 107, 156
Jain, B., & Seljak, U. 1997, ApJ, 484, 560
Jarvis, J. F., & Tyson, J. A. 1981, AJ, 86, 476
Kaiser, N. 1996, preprint (astro-ph/9610120)
———. 1999, preprint (astro-ph/9904003)
Kaiser, N., Squires, G., & Broadhurst, T. 1995, ApJ, 449, 460 (KSB)
Kneib, J.-P., Ellis, R. S., Smail, I., Couch, W. J., & Sharples, R. M. 1996, ApJ, 471, 643
Krist, J., & Hook, R. 1997, The Tiny Tim User's Guide (Baltimore: STScI)
Kuijken, K. 1999, A&A, 352, 355
Luppino, G. A., & Kaiser, N. 1997, ApJ, 475, 20 (LK)
Mellier, Y. 1999, ARA&A, 37, 127
Narayan, R., & Bartelmann, M. 1996, preprint (astro-ph/9606001)
Refregier, A. 1999, Weak Lensing by Large-Scale Structure: Links and Bibliography, unpublished[4]
Refregier, A., Brown, S. T., Kamionkowski, M., Helfand, D. J., Cress, C. M., Babul, A., Becker, R., & White, R. L. 1998, in Wide-Field Surveys in Cosmology, Proc. XIVth IAP Meeting, ed. Y. Mellier & S. Colombi (Paris: Editions Frontières), 209
Rhodes, J. 1999, Ph.D. thesis, Princeton Univ.
Rhodes, J., Groth, E., & WFPC1 IDT. 1997, BAAS, 29, 1207
Richer, H. B., et al. 1997, ApJ, 484, 741
Schneider, P., Ehlers, J., & Falco, E. E. 1992, Gravitational Lenses (New York: Springer)
Schneider, P., & Seitz, C. 1995, A&A, 294, 411
Schneider, P., van Waerbeke, L., Mellier, Y., Jain, Y., Seitz, S., & Fort, B. 1997, preprint (astro-ph/9705122)
Stebbins, A., McKay, T., & Frieman, J. A. 1996, Proc. IAU Symp. 173, Astrophysical Applications of Gravitational Lensing, ed. C. S. Kochanek & J. N. Hewitt (Dordrecht: Kluwer), 75
van Waerbeke, L., Bernardeau, F., & Mellier, Y. 1999, A&A, 342, 15
Villumsen, J. 1995, preprint (astro-ph/9507007)

[4] Available at http://www.astro.princeton.edu/~refreg.